

Angular momentum of vacuum bubbles in a first-order phase transition

Jan Tristram Acuña,^a Danny Marfatia,^b Po-Yan Tseng^{a,c}

^aDepartment of Physics, National Tsinghua University, 101 Kuang-Fu Rd., Hsinchu 300044, Taiwan ROC

^bDepartment of Physics and Astronomy, University of Hawai'i, Honolulu, HI 96822, USA

^cPhysics Division, National Center for Theoretical Sciences, Taipei 106319, Taiwan ROC

E-mail: jtacuna@gapp.nthu.edu.tw, dmarf8@hawaii.edu,
pytseng@phys.nthu.edu.tw

Abstract. The formation of primordial black holes (PBHs) during a first-order phase transition (FOPT) in a dark sector has been of recent interest. A quantity that characterizes a black hole is its spin. We carry out the first step towards determining the spin of such PBHs, by calculating the spin of spherical false vacuum bubbles induced by cosmological perturbations. The angular momentum is given by the product of density and velocity perturbations. We carefully track the evolution of background quantities and calculate the transfer functions during the FOPT. We find that the dimensionless spin parameter $s = J/(G_N M^2)$ of false vacuum bubbles of mass M and angular momentum J , take a wide range of values from $\mathcal{O}(10^{-3})$ to $\mathcal{O}(10^3)$ for FOPTs between 10 keV and 100 GeV and a dark sector that is 0.1 to 0.4 times cooler than the visible sector. We also find a scaling relation between the root-mean-square value of the spin, the FOPT time scale, the bubble wall velocity, and the dark sector-to-visible sector temperature ratio.

Contents

1	Introduction	1
2	Dark first-order phase transitions	3
2.1	Physical conditions	6
3	Angular momentum from cosmological perturbations	8
3.1	Angular momentum in general relativity	8
3.2	Angular momentum in a perturbed FRW spacetime	11
3.3	Spin of primordial black holes	15
3.4	Angular momentum due to uniform pressure	16
4	Evolution of cosmological perturbations	16
4.1	Evolution of perturbations: η_0 to η_c	17
4.2	Evolution of perturbations: η_c to η_*	19
4.2.1	Background evolution	19
4.2.2	Parameter selection and scans over physical FOPT scenarios	26
4.2.3	Perturbations during a FOPT	28
4.2.4	Superhorizon and subhorizon limits	31
4.2.5	Numerical scheme	33
5	Results and discussion	39
5.1	Numerical values of physical quantities	39
5.2	Estimates and scans over the physical region	39
5.3	Benchmarks	42
6	Conclusions	44

1 Introduction

A well-known result in general relativity (GR) is that black holes can be characterized by their mass and spin. As discussed extensively in the literature, the angular momentum of primordial black holes (PBHs) is strongly related to the black hole production mechanism. A common scenario is that enhancements in the primordial curvature power spectrum increase the probability of obtaining rare density peaks above the critical threshold for collapse [1–4]. Computations of the spin of PBHs have been performed adopting various hypotheses, where they predict spin values in the range $s \simeq 10^{-3} \sim 10^{-2}$ [5–8]. Alternatively, we focus on the scenario that PBHs are formed from a cosmological dark first-order phase transition (FOPT) without any enhancement in the primordial power spectrum.

The PBH may be formed from the direct collapse of false vacuum (FV) bubbles [9]. Another mechanism involves the formation of intermediate compact objects called Fermi balls (FBs), which are composed of degenerate dark fermions [10, 11]. The FBs cool down by emitting light particles that may eventually trigger the collapse into PBHs. Both mechanisms efficiently produce subsolar mass FBs/PBHs for FOPT energy scales from $\mathcal{O}(\text{keV})$ to $\mathcal{O}(100 \text{ GeV})$. In this work, the fundamental hypothesis in generating PBH spin is the

idea that cosmological perturbations induce nonzero angular momentum. The cosmological perturbations are Gaussian random variables whose initial values are ultimately determined by the primordial curvature power spectrum. We show that the angular momentum and spin are Gaussian random variables and thus their distributions are determined by their root-mean-square (RMS) values. We restrict our calculation of the spin to the case of false vacuum (FV) bubbles for a number of reasons. In the case of direct collapse to PBHs, the process is nonlinear and may require techniques beyond perturbation theory. Similarly, in the case where FBs are formed, the emission of light species carry away angular momentum from the FV bubble. Tracking the subsequent evolution of the angular momentum is beyond the scope of our work.

In order to realize the FOPT scenario, which is an essential ingredient in the novel PBH formation mechanism that we feature in this work, it is necessary to introduce dark sector dynamics, since phase transitions in the Standard Model are known to be smooth crossovers. In particular, we consider a model framework with a dark scalar ϕ that triggers the FOPT. For the case where the intermediate step of forming Fermi balls is present, we also require the presence of a dark Dirac fermion χ , which will serve as the fundamental building block for Fermi balls. The size distribution of FV bubbles during the FOPT has been discussed in Ref. [12], from which the mass and abundance of FB/PBH can be determined. In our work, we take the size of the FV sphere to be the critical radius at the time of percolation, within which no true vacuum bubble can nucleate.

Earlier studies on PBH formation from FOPTs focused on the PBH mass and have not considered the generation of angular momentum. In this setup, it would be possible to generate angular momentum from spatial inhomogeneities in the wall velocity, or from perturbations in the density and velocity fields of the fluid component forming the FV bubble. For this work, we adopt the latter approach, where we track the density, velocity, and metric perturbations from the time in which all modes are superhorizon, up to the time of percolation during the FOPT. We assume that the initial conditions are set by Gaussian primordial curvature perturbations, that are nearly scale-invariant. We adopt the uniform Hubble gauge to track the evolution of the perturbations. Taking into account some subtleties in defining angular momentum in GR, we express the angular momentum as a volume integral of a product of density and velocity perturbations, where we choose the volume of the proto-object to be spherical. As mentioned, the angular momentum and spin are random variables since the initial curvature perturbations are themselves Gaussian random variables. Thus, our goal is to calculate the RMS spin of FV bubbles during a dark FOPT at the time of percolation.

We point out that the determination of the PBH spin, as well as its distribution, has been the subject of active investigation in the literature. Based on the seminal work [13] on the critical behavior of BH masses, arising from the evolution of a family of ingoing packets of a scalar field, Ref. [14] considered a radiation fluid characterized by the size of the density fluctuation and angular momentum. The main result of [14] is the presence of a power-law relation not only for the BH mass but also for the angular momentum. Building upon this work, Ref. [15] obtained the mass and angular momentum distribution by assuming that the initial density fluctuation is Gaussian, while the parameter describing the initial rotation was assumed to be flat. The resulting spin is around $s < 0.4$; on the other hand, accretion effects on the mass and spin of the BHs were shown to be negligible. In the case where the PBH spin is induced by cosmological perturbations Ref. [5] calculated the RMS value of the PBH spin, assuming that the PBHs are formed from the collapse of rare spherically

symmetric density peaks. The spin of the PBH was shown to be a product of density and velocity perturbations, making it a *second-order* quantity in perturbations. Assuming a narrow enhancement in the primordial curvature power spectrum, they obtained $s \simeq 0.01$, for PBHs comprising a sizable fraction of dark matter. In contrast, Ref. [6] assumed that the proto-object that will eventually collapse into PBHs is ellipsoidal, and the distribution of the ellipsoidal configurations is determined by peak theory [16]. They showed that the PBH spin is a *first-order* quantity in perturbations and obtained spin parameters at the percent level, given some assumptions in the enhancement in the curvature power spectrum. Ref. [7] followed the formalism laid down in Ref. [6], and provided some improvements in the analysis of the latter. Both approaches assumed that the initial PBH spin corresponds to the value at turn around time, *i.e.*, the moment when the overdensity begins to collapse; in Ref. [17], they pointed out that the turn around time does not necessarily occur at the moment when the (enhanced) perturbation mode enters the horizon. As a result, Ref. [17] predicted an RMS spin value of $\simeq 4.0 \times 10^{-3} (M/M_H)^{-1/3}$, where M_H is the mass within the Hubble horizon at horizon entry of the enhanced perturbation. In addition, Ref. [17] pointed out that the second-order approach in Ref. [5] may give rise to spin estimates that are comparable with the first-order approach. In Ref. [18], PBHs are formed from the collapse of domain walls and the angular momentum arises from the tidal forces from the surrounding radiation fluid acting on the walls, obtaining $s \simeq 10^{-4} (M/30M_\odot)^{-1}$. Finally, recent work in Ref. [8] used the result from Ref. [6], and combined it with the curvature perturbation obtained in Ref. [19, 20], where they obtained a spin value of around $s \simeq \mathcal{O}(10^{-3})$. The curvature perturbation is generated from the difference in nucleation times of different points in space, thereby generating regions that contain more vacuum energy than others. We point out that the applicability of the result from Ref. [6] assumes that any modification in the curvature power spectrum should be made at the time when all perturbations are superhorizon.

The rest of the paper will be devoted to the task of calculating the spin of FV bubbles at the percolation time, during a FOPT in the dark sector, induced by cosmological perturbations. In Section 2 we first introduce the dark sector model and the quartic scalar potential, before proceeding with the discussion of angular momentum in GR and in the specific case of a perturbed FRW spacetime in Section 3. Following Ref. [21], we present the evolution equations for cosmological perturbations in the uniform Hubble gauge in Section 4. We separately consider the period from the time when all modes are superhorizon up to the critical point, and the period of FOPT between the critical point and the percolation time. Determining the evolution of the background quantities and the perturbations during the FOPT are crucial to our task, and we provide a detailed discussion of this part of the calculation in Section 4.2. We present our main results, estimates for the FV spin, and benchmark points in Section 5. Finally, we conclude in Section 6.

2 Dark first-order phase transitions

In the case where PBHs are formed from the direct collapse of FV bubbles, it is sufficient to consider only a real scalar field ϕ in the dark sector. The scalar field triggers the FOPT by acquiring a nonzero expectation value at some critical point. On the other hand, if we consider the formation of Fermi balls, we also need to add Dirac dark fermions χ in the particle spectrum. These fermions serve as the fundamental component of Fermi balls. Then

the dark sector effective Lagrangian density can be written as

$$\mathcal{L} = \frac{1}{2} (\partial\phi)^2 - V_{\text{eff}}(\phi, T) + \bar{\chi} (i\not{\partial} - m_\chi) \chi - g_\chi \phi \bar{\chi} \chi, \quad (2.1)$$

where T is the temperature of the dark sector, and the effective potential is given by

$$V_{\text{eff}}(\phi, T) = V_4(\phi, T) - \frac{\pi^2}{90} g_\rho(\phi) T^4 - \Delta b(\phi) T^2 \phi^2, \quad (2.2)$$

where the quartic potential is

$$V_4(\phi, T) = \frac{\lambda}{4} \phi^4 - (AT + C) \phi^3 + D(T^2 - T_0^2) \phi^2. \quad (2.3)$$

The form of the effective potential may arise from a more fundamental theory, possibly with more particle species, where the usual procedure of accounting for the zero-temperature and finite-temperature contributions to the effective potential at one-loop order, and taking the high-temperature limit are carried out, as in Refs. [22, 23]. The quantity $g_\rho(\phi)$ just counts the number of effective relativistic degrees of freedom in the dark sector for a given classical field configuration ϕ , where bosons and fermions are respectively weighted by 1 and 7/8. Meanwhile, Δb counts the number of degrees of freedom that are relativistic in the false vacuum but not in the true vacuum (TV). For simplicity, we take

$$\Delta b = 0, \quad g_\rho = 4.5. \quad (2.4)$$

We take λ , A , C , D , and T_0^2 to be positive real parameters and require that $T > T_0$ so that the potential has two minima with one at $\phi = 0$. At the critical temperature $T = T_c$, the two minima are degenerate in energy. When the temperature of the dark sector further cools to $T < T_c$, the $\phi = 0$ configuration will be regarded as the false vacuum, which has a higher energy than the other minimum, the true vacuum, given by

$$\phi_+(T) = \frac{3(AT + C) + \sqrt{9(AT + C)^2 - 8\lambda D(T^2 - T_0^2)}}{2\lambda}. \quad (2.5)$$

During this period, regions of spacetime will begin to nucleate TV bubbles, at a rate per unit volume given by the nucleation rate Γ , which depends on the underlying particle physics model. The bubbles of TV expand, and the TV bubbles subsequently form an infinite connected network of bubbles, which defines the time of *percolation*. A useful criterion for calculating the percolation time is to identify the FV fraction F , defined as the spatial volume fraction occupied by FV bubbles, with $1/e$.

Note that the Yukawa term in Eq. (2.1) is mainly relevant for the Fermi ball scenario of PBH formation, but it can also be present in the scenario where PBHs are directly formed from FV bubbles. Firstly, the Yukawa term allows the filtered DM scenario to be realized, where the χ species are trapped inside FV bubbles. A necessary condition for this to occur is that the χ mass difference $\Delta m_\chi = g_\chi \phi_+$ between the TV and FV is much larger than the typical kinetic energy of χ , roughly given by T , so that the flux of χ particles through the bubble walls is exponentially suppressed. Secondly, the Yukawa term provides an attractive force between the χ particles to trigger an instability that leads to the formation of PBH from FBs. Finally, under certain conditions, the Yukawa interaction ensures that the χ and ϕ species are tightly coupled with each other. The necessary condition for this to occur can

be derived by requiring that interactions involving χ and ϕ , *e.g.* $\chi\bar{\chi} \rightarrow \phi\phi$, occur at a much faster rate than the Hubble expansion, so that we have

$$\frac{n_\chi \langle \sigma v \rangle_{\chi\bar{\chi} \rightarrow \phi\phi}}{H} \sim g_{\rho, \text{SM}} g_\chi^4 r_T \frac{M_{\text{Pl}}}{T_{\text{SM}}} \gg 1, \quad (2.6)$$

where $r_T \equiv T/T_{\text{SM}}$ is the dark-to-SM-sector temperature ratio, and $g_{\rho, \text{SM}}$ is the effective number of relativistic degrees of freedom in the SM sector at temperature T_{SM} .

The dynamics of the FOPT is determined by tracking the cosmological evolution of the plasma, in the presence of both SM and dark sector degrees of freedom, treating each component as a fluid with a known equation of state. For the dark sector we can calculate the thermodynamic quantities—free energy, pressure, entropy, and energy—in the false and true vacuum using the effective potential Eq. (2.2). These are then given respectively by (cf. [24–27])

$$\mathcal{F}_{\text{FV}}(T) = -\frac{\pi^2}{90} g_\rho T^4, \quad \mathcal{F}_{\text{TV}}(T) = -\frac{\pi^2}{90} g_\rho T^4 + \Delta p(T), \quad (2.7)$$

$$p_{\text{FV}}(T) = \frac{\pi^2}{90} g_\rho T^4, \quad p_{\text{TV}}(T) = \frac{\pi^2}{90} g_\rho T^4 - \Delta p(T), \quad (2.8)$$

$$s_{\text{FV}}(T) = \frac{2\pi^2}{45} g_\rho T^3, \quad s_{\text{TV}}(T) = \frac{2\pi^2}{45} g_\rho T^3 - \Delta s(T), \quad (2.9)$$

$$\rho_{\text{FV}}(T) = \frac{\pi^2}{30} g_\rho T^4, \quad \rho_{\text{TV}}(T) = \frac{\pi^2}{30} g_\rho T^4 - \Delta \rho(T), \quad (2.10)$$

where

$$\Delta p = -\Delta V(T), \quad \Delta s = \frac{d}{dT} \Delta p = -\frac{d\Delta V(T)}{dT}, \quad \Delta \rho = T\Delta s - \Delta p = \Delta V(T) - T \frac{d\Delta V(T)}{dT}. \quad (2.11)$$

To simplify our analysis, we match the thermodynamic quantities with the *bag model* [25], by expanding $\Delta V(T)$ about the critical temperature T_c , up to linear order. By definition, the critical temperature is the moment at which $\Delta p = 0$, so that $\Delta V(T_c) = 0$. In terms of the parameters in the quartic potential,

$$(A^2 - \lambda D) T_c^2 + 2ACT_c + (C^2 + \lambda DT_0^2) = 0. \quad (2.12)$$

We can trade the D parameter in exchange for T_c via

$$\lambda D = \frac{\left(A + \frac{C}{T_c}\right)^2}{1 - \frac{T_0^2}{T_c^2}}. \quad (2.13)$$

Meanwhile, the derivative of Δp is discontinuous at $T = T_c$. This is simply attributed to the presence of a latent heat, which is a defining characteristic of a first-order phase transition. Denoting the latent heat at the critical temperature by L_c , where

$$\Delta \rho(T_c) = L_c, \quad (2.14)$$

we have

$$\Delta p(T) \approx -L_c \left(1 - \frac{T}{T_c}\right), \quad \Delta s(T) \approx \frac{L_c}{T_c}, \quad \Delta \rho(T) \approx L_c. \quad (2.15)$$

In terms of the parameters in the effective potential, we have

$$L_c \equiv -T \frac{d\Delta V(T)}{dT} \Big|_{T=T_c} = T_c^4 \frac{8(A+x_C)^3 (AT_0^2/T_c^2 + x_C)}{\lambda^3 (1 - T_0^2/T_c^2)}, \quad x_C \equiv \frac{C}{T_c}. \quad (2.16)$$

This quantity roughly tells us the amount of energy that will be liberated during the transition from the false vacuum to true vacuum. Note that Eq. (2.16) can be inverted to give

$$\frac{T_0^2}{T_c^2} = \frac{\lambda^3 (L_c/T_c^4) - 8x_C(A+x_C)^3}{\lambda^3 (L_c/T_c^4) + 8A(A+x_C)^3}. \quad (2.17)$$

Since $0 \leq T_0^2/T_c^2 \leq 1$, there must be a lower bound for the latent heat, *i.e.*

$$\frac{L_c}{T_c^4} \geq \frac{8x_C(A+x_C)^3}{\lambda^3}. \quad (2.18)$$

2.1 Physical conditions

We further impose physical conditions on the thermodynamic quantities, to restrict the class of effective potentials that will be the subject of this study. These conditions should apply for all temperatures within $T_0 \leq T \leq T_c$. In the bag model, $\Delta p = -L_c(1 - T/T_c) \leq 0$ is automatically satisfied, which ensures that the TV regions exert a net outward pressure on the surrounding FV region, to allow nucleated TV bubbles to expand. Furthermore, we require $\Delta\rho \geq 0$ since the FV has a higher energy than the TV. This translates to

$$\frac{\pi^2}{30} g_\rho T_0^4 \geq L_c, \quad (2.19)$$

so that

$$\frac{L_c}{T_c^4} \leq \frac{\pi^2}{30} g_\rho T_0^4 / T_c^4. \quad (2.20)$$

It can be easily seen that the rescaled latent heat L_c/T_c^4 cannot be increased indefinitely. Suppose we take a large value of L_c/T_c^4 , so that $T_0^2/T_c^2 \rightarrow 1$ according to Eq. (2.17). But the right hand side of Eq. (2.20) suggests that L_c/T_c^4 cannot exceed $g_\rho \pi^2/30$. Analogously, the greatest lower bound for the rescaled latent heat must be larger than the one prescribed in Eq. (2.18) which leads to $T_0^2/T_c^2 = 0$, because of Eq. (2.20). In addition, the square of the sound speed in the TV, taken in isolation, differs from that of a radiation fluid, and is given by

$$c_{s,\text{TV}}^2 = \frac{dp_{\text{TV}}/dT}{d\rho_{\text{TV}}/dT} \simeq \frac{1}{3} \left[1 - \frac{15}{\pi^2 g_\rho} \left(\frac{L_c}{T_c^4} \right) \left(\frac{T}{T_c} \right)^{-3} \right]. \quad (2.21)$$

One can check that the physical condition Eq. (2.20) guarantees that $c_{s,\text{TV}}^2$ remains positive and subluminal. In general, Eq. (2.20) can be recast using Eq. (2.17) as

$$\gamma u^3 - u^2 + \gamma b u + a < 0, \quad \gamma \equiv \left(\frac{30}{\pi^2 g_\rho} \right)^{1/2}, \quad u \equiv \left(\frac{L_c}{T_c^4} \right)^{1/2}, \quad (2.22)$$

$$a \equiv \frac{8x_C(A+x_C)^3}{\lambda^3}, \quad b \equiv \frac{8A(A+x_C)^3}{\lambda^3}. \quad (2.23)$$

For a given pair of A and x_C , the problem is reduced to solving the roots of the cubic polynomial. We want the case where we have two positive real roots, which will determine the allowed range of L_c/T_c^4 . It is easy to show that there is always one negative real root, while there can be two or no positive real roots.

We find it convenient to consider

$$A, \quad T_c, \quad \lambda, \quad \frac{L_c}{T_c^4}, \quad x_C$$

as fundamental parameters. Once these parameters are specified, the effective potential is known. In choosing our benchmark points, we take $A = 10^{-1}, 10^{-2}, 10^{-3}, 10^{-4}$. As for the other parameters, we turn to the physical conditions for guidance. It turns out that there is an absolute minimum value of $\lambda = \lambda_0$, below which there exists no physical parameter region in the $(L_c/T_c^4, x_C)$ plane. This can be obtained by setting the discriminant of the cubic polynomial in Eq. (2.22) to zero, *i.e.*

$$\frac{1}{\lambda^3} \cdot \left[c_2 \left(\frac{1}{\lambda^3} \right)^2 + c_1 \left(\frac{1}{\lambda^3} \right) + c_0 \right] = 0, \quad (2.24)$$

$$c_2 \equiv 55296A^3(A + x_C)^9\gamma^6, \quad (2.25)$$

$$c_1 \equiv -1728(A + x_C)^6(A^2 - 18Ax_C - 27x_C^2)\gamma^4, \quad (2.26)$$

$$c_0 \equiv -864x_C(A + x_C)^3\gamma^2, \quad (2.27)$$

and then setting $x_C = 0$. We find that

$$\lambda_0 = (32A^4\gamma^2)^{1/3} \simeq 0.129 \left(\frac{A}{0.1} \right)^{4/3} \left(\frac{4.5}{g_\rho} \right)^{1/3}. \quad (2.28)$$

For given values of A and λ , the values of x_C and L_c/T_c^4 are chosen to lie in the physical region, such that Eq. (2.22) is satisfied. On the other hand, if we choose A and λ , then Eq. (2.24) becomes a polynomial equation for the maximum x_C that can accommodate physical values of L_c/T_c^4 .

Note that statements regarding the physical condition are independent of T_c , which only sets the scale of the phase transition. In the following, we take

$$T_c = 10 \text{ keV}, 1 \text{ MeV}, 10 \text{ MeV}, 1 \text{ GeV}, 100 \text{ GeV}.$$

As an illustration, in Fig. 1 we show the physical region as unshaded, for $A = 0.1, 0.001$, choosing two values of λ/λ_0 for each: 1.42 and 2.34. The black line corresponds to $T_0 = 0$, so that the region above it leads to $T_0^2 < 0$, and is thus forbidden. The green contours correspond to contours of constant $T_0/T_c = 0.1, 0.2, \dots$, to 0.9, indicated by solid curves. We also show contours where T_0/T_c is very close to unity, with $T_0/T_c = 1 - 10^{-2}, 1 - 10^{-3}, \dots$, indicated by dashed curves. Meanwhile, the shaded red region corresponds to FOPT scenarios that are excluded by the physical condition $\rho_{\text{TV}} < 0$, for all $T_0 \leq T \leq T_c$. The horizontal dashed line marks the maximum x_C value allowed under this physical condition, for fixed A and λ . We also observe that a smaller x_C leads to a wider range of allowed L_c/T_c^4 values. The maximum range of physical L_c/T_c^4 values is achieved when $x_C = 0$, for fixed A and λ .

Note that a larger λ leads to a larger area occupied by the physical region, as well as an increase in the maximum x_C . Smaller values of L_c/T_c^4 are accommodated, opening up a wider range of physical rescaled latent heat values.

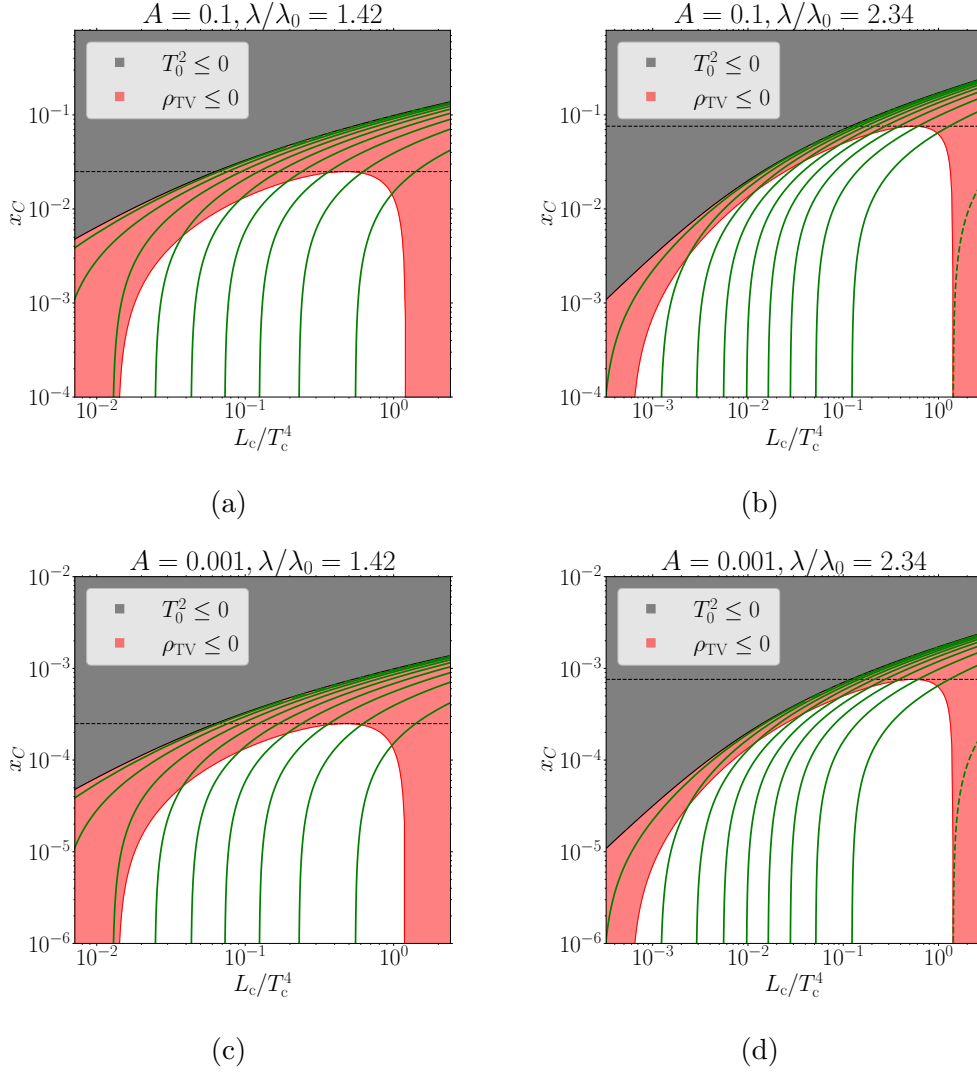


Figure 1. The physical region for $A = 0.1, 0.001$, and two values of $\lambda/\lambda_0 = 1.42, 2.34$. The green curves correspond to contours of constant T_0/T_c . For all cases, $g_\rho = 4.5$.

3 Angular momentum from cosmological perturbations

In our approach, we would like to estimate the angular momentum of a volume enclosing a dark fluid, induced by cosmological perturbations. We assume that these volumes are spherical to simplify our calculations. To set up the starting expression for the angular momentum, we first provide a discussion of some well-known subtleties regarding its definition in GR (cf. [28–32]).

3.1 Angular momentum in general relativity

In flat spacetime, the mass M and angular momentum J^c of an isolated system can be constructed from the energy momentum tensor, and are just the components of tensors,

expressed in terms of volume integrals, given by

$$P^\mu = \int_{\mathcal{V}} d^3\vec{x} T^{0\mu}, \quad J^{\mu\nu} = \int_{\mathcal{V}} d^3\vec{x} (x^\mu T^{0\nu} - x^\nu T^{0\mu}), \quad (3.1)$$

Specifically, $M = P^0$ and $J_c = 1/2 \epsilon_{abc} J^{ab}$. The above quantities are conserved, owing to the fact that

$$\partial_\mu T^{\mu\nu} = 0. \quad (3.2)$$

Furthermore, one can show that the total mass and angular momentum reduce into surface integrals. This follows from the linearized field equations, expanded about Minkowski spacetime, which can be written as [29]

$$\partial_\alpha \partial_\beta H^{\mu\alpha\nu\beta} = 16\pi G_N T^{\mu\nu}, \quad (3.3)$$

where $H^{\mu\alpha\nu\beta}$ is quantity with the same symmetries as the Riemann tensor, and which also depends on the linearized metric

$$g_{\alpha\beta} \approx \eta_{\alpha\beta} + h_{\alpha\beta}, \quad |h_{\alpha\beta}| \ll 1. \quad (3.4)$$

The conservation of $T^{\mu\nu}$ trivially follows from the symmetries of H and the linearized field equations. Explicitly, we then have

$$P^\mu = \frac{1}{16\pi G_N} \oint_{\partial\mathcal{V}} \partial_i H^{\mu i 0j} n_j dS, \quad (3.5)$$

$$J^{\mu\nu} = \frac{1}{16\pi G_N} \oint_{\partial\mathcal{V}} \left(x^\mu \partial_\beta H^{\nu\beta 0j} - x^\nu \partial_\beta H^{\mu\beta 0j} + H^{\mu j 0\nu} - H^{\nu j 0\mu} \right) n_j dS. \quad (3.6)$$

Note that even in the linearized case, the integrands of the flux integrals are gauge-dependent, because we have the freedom to choose a coordinate system where the derivatives of the metric vanish. However, the surface integrals are defined at the boundary where the spacetime is Minkowski, and hence the quantities P^μ and $J^{\mu\nu}$ behave as tensors, and this presents no ambiguity regarding the values of M and J^c . In a generic spacetime, however, the energy momentum tensor $T^{\mu\nu}$ is covariantly conserved, *i.e.*

$$\nabla_\mu T^{\mu\nu} = \frac{1}{\sqrt{-g}} \partial_\mu (\sqrt{-g} T^{\mu\nu}) + \Gamma_{\alpha\beta}^\nu T^{\alpha\beta} = 0, \quad (3.7)$$

where ∇_μ is the covariant derivative associated with the Christoffel connection $\Gamma_{\alpha\beta}^\nu$. This does not automatically imply the existence of a global conservation law. Intuitively, this can be traced back to the fact that the gravitational field itself, not just the matter fields, generates energy. Heuristically, the contribution of the gravitational field to the total energy momentum is expected to involve a product of metric derivatives, by analogy with the Newtonian case where the energy density is the square of the gradient of the gravitational potential. Then one can construct a quantity $\tau_{\mu\nu}$, which represents the stress energy of the gravitational field, such that, when combined with the matter stress energy tensor $T^{\mu\nu}$, yields a global conservation law. As an example, Landau and Lifshitz [28] constructed (see also [33] for a unified treatment in terms of superpotentials [34–38]; not to be confused with the superpotential in supersymmetry)

$$\tau_{(\text{LL})}^\alpha{}_\lambda + \sqrt{-g} T^\alpha{}_\lambda = \partial_\beta \left(\sqrt{-g} U_\lambda^{\alpha\beta} \right), \quad (3.8)$$

where

$$U_{\lambda}^{\alpha\beta} \equiv \frac{1}{16\pi G_N \sqrt{-g}} g_{\lambda\kappa} \partial_{\sigma} \left[g(g^{\alpha\sigma} g^{\beta\kappa} - g^{\beta\sigma} g^{\alpha\kappa}) \right]. \quad (3.9)$$

We make a few comments about τ . Notice that U is antisymmetric in α and β , so that the left hand side of Eq. (3.8) follows a conservation law. We also note that $\tau_{(\text{LL})}$ is not a tensor, but rather a pseudotensor, because it only transforms as a tensor under a subset of general coordinate transformations. Furthermore, as in the case of linearized gravity, there exists a coordinate system such that $U_{\lambda}^{\alpha\beta} = 0$, so that $\tau_{(\text{LL})}$ is inherently ambiguous and coordinate dependent; nevertheless, when τ is contracted with the normal of a timelike hypersurface, and then integrated over a volume that extends to spatial infinity, the value is unambiguous, assuming that the spacetime is asymptotically flat. Finally, the form of τ is not uniquely determined and there are other constructions that lead to a globally conserved quantity. Then from the energy momentum pseudotensor, one can define angular momentum as

$$J_i = \epsilon_{ijk} \int_{\mathcal{V}} d^3\vec{x} \, x^j \left[\tau_{(\text{LL})}^{0k} + \sqrt{-g} T^{0k} \right], \quad (3.10)$$

and this can be rewritten as a surface integral, like in the case of linearized gravity. If the spacetime is asymptotically flat, then taking the boundary to spatial infinity ensures that J_i will be meaningful and unambiguous.

An alternative procedure to obtain conserved quantities is to exploit the presence of symmetries in a given spacetime. If there exists a Killing vector ξ^{μ} satisfying

$$\nabla_{\mu} \xi_{\nu} + \nabla_{\nu} \xi_{\mu} = 0, \quad (3.11)$$

one can construct globally conserved quantities. Note that the quantity $T_{\beta}^{\alpha} \xi^{\beta}$ is covariantly conserved, which implies that

$$\partial_{\alpha} \left(\sqrt{-g} T_{\beta}^{\alpha} \xi^{\beta} \right) = 0. \quad (3.12)$$

In particular, stationary and axisymmetric spacetimes admit a timelike Killing vector $\xi_{(t)}$, associated with time translation symmetry, and a spacelike Killing vector $\xi_{(\phi)}$, associated with rotation isometry. Then the Komar mass and angular momentum are given by integrals over a codimension-2 surface, corresponding to the boundary of a timelike hypersurface Σ with a normal vector n^{μ} . Explicitly these are given by

$$M = -\frac{1}{8\pi G_N} \oint_{\partial\Sigma} \nabla^{\mu} \xi_{(t)}^{\nu} dS_{\mu\nu}, \quad J = \frac{1}{16\pi G_N} \oint_{\partial\Sigma} \nabla^{\mu} \xi_{(\phi)}^{\nu} dS_{\mu\nu}, \quad (3.13)$$

where

$$dS_{\mu\nu} = (s_{\mu} n_{\nu} - s_{\nu} n_{\mu}) \sqrt{\gamma} d^2 y \quad (3.14)$$

is the surface element on $\partial\Sigma$, with spacelike normal s_{μ} , induced metric γ , and coordinates y^a installed on it. It is assumed that the spacetime is asymptotically flat and the exterior region is vacuum. In terms of hypersurface integrals, we have

$$M = 2 \int_{\Sigma} \left(T_{\mu\nu} - \frac{1}{2} g_{\mu\nu} T \right) n^{\mu} \xi_{(t)}^{\nu} \sqrt{g_3} d^3 \vec{x}, \quad (3.15)$$

$$J = - \int_{\Sigma} \left(T_{\mu\nu} - \frac{1}{2} g_{\mu\nu} T \right) n^{\mu} \xi_{(\phi)}^{\nu} \sqrt{g_3} d^3 \vec{x}, \quad (3.16)$$

where g_3 is the determinant of the induced metric on Σ . We note that the angular momentum in Eq. (3.15) was adopted in [6] to calculate the spin of PBHs in a flat FRW background. In the case of a perturbed FRW background however, there is no Killing vector associated with rotational symmetry to begin with. Nevertheless, globally conserved quantities can still be defined in the case of perturbed spacetimes.

3.2 Angular momentum in a perturbed FRW spacetime

The discussion in [39] will be useful for our task in determining the angular momentum of fluids subjected to cosmological perturbations, where they constructed conserved charges based on the seminal work [37]. Reference [39] formulated a procedure to obtain superpotentials and conserved quantities, followed by an application of the formalism in the case of perturbed FRW backgrounds. We refer the interested reader to [39] for the explicit expressions for the superpotentials and conserved quantities in a general curved spacetime, and instead we only quote the relevant results. Consider a flat FRW background endowed with a metric $\bar{g}_{\mu\nu} = a^2(\eta)\eta_{\mu\nu}$, and ξ are chosen to be the 15 conformal Killing vectors of Minkowski spacetime—4 spacetime translations, 3 from spatial rotations, 3 from Lorentz boosts, 1 from dilation and 4 from special conformal transformations. Taking the time component of the conserved quantity \hat{I}^μ , with an associated superpotential $\hat{I}^{\mu\nu}$, we have

$$8\pi G_N \hat{I}^{0i} = \frac{1}{2}a^2 \left[\left(2\mathcal{H}\tilde{l}^{0i} - \partial^k q_k^i \right) \xi^0 + q_k^i \partial^k \xi^0 + Q_k^i \xi^k + \tilde{l}_k^0 \partial^{[k} \xi^{i]} \right], \quad (3.17)$$

$$\hat{I}^0 = \partial_i \hat{I}^{0i}, \quad \tilde{l}^{\mu\nu} \equiv \frac{1}{a^2} (\sqrt{-g}g^{\mu\nu} - \sqrt{-\bar{g}}\bar{g}^{\mu\nu}), \quad (3.18)$$

where

$$\mathcal{H} \equiv \frac{1}{a} \frac{da}{d\eta}, \quad q_l^m \equiv \delta_l^m \tilde{l}^{00} - \tilde{l}_l^m, \quad (3.19)$$

$$Q_l^m \equiv \partial^m \tilde{l}_l^0 - \partial_0 q_l^m - \delta_l^m \left[\partial^n \tilde{l}_n^0 + \mathcal{H} (\tilde{l}_n^n + \tilde{l}^{00}) \right]. \quad (3.20)$$

Note that Eqs. (3.17)-(3.20) are exact expressions, even for “large” perturbations of the background FRW metric \bar{g} . Note that the Latin indices are raised and lowered using the Kronecker delta. Typically, we are interested in the volume integral of \hat{I}^0 over a spherical volume at a given conformal time η . Ref. [39] demonstrated that the conserved charges are gauge dependent, and these quantities take on simpler forms in the uniform Hubble gauge [21, 40–42], where the change in the trace of the extrinsic curvature of surfaces of constant conformal time, under metric perturbations, is zero. In this gauge, the perturbed FRW metric in comoving coordinates can be written as [21, 40]

$$ds^2 = -(1 + 2\Psi)dt^2 + a^2(t) [\delta_{ij}(1 + 2\Phi) + 2\partial_i \partial_j \gamma] dx^i dx^j. \quad (3.21)$$

One can also quickly arrive at the realization that the angular momentum due to cosmological perturbations is a gauge dependent quantity, by noting that the velocity perturbations vanish in the comoving gauge, so that the angular momentum goes to zero. Since we are particularly interested in the angular momentum, the relevant Killing vectors are ξ_i associated with rotation symmetry, with coordinate basis components,

$$(\xi_i)_b = \epsilon_{iab} x^a. \quad (3.22)$$

The subscript i refers to the direction along the i axis. Then the corresponding superpotential takes a simpler form,

$$8\pi G_N(\hat{I}_i)^{0j} = \frac{1}{2}a^2 \left(Q^{jk}\epsilon_{iak}x^a + \tilde{l}^{0k}\epsilon_{ikj} \right). \quad (3.23)$$

To first order in perturbations, one finds

$$q_l^m \simeq \tilde{h}_l^m - \delta_l^m \tilde{h}_n^n, \quad Q_l^m \simeq \left(2\mathcal{H}\tilde{h}_{00} - \partial^n \tilde{h}_{0n} \right) \delta_l^m + \partial^m \tilde{h}_{0l} - \partial_0 q_l^m, \quad (3.24)$$

where $a^2 \tilde{h}_{\mu\nu} = g_{\mu\nu} - \bar{g}_{\mu\nu}$. The corresponding density is then

$$(\hat{I}_i)^0 \simeq a \delta T^{0k} \epsilon_{ijk} x^j \sqrt{\bar{g}_3}. \quad (3.25)$$

For a spherical volume \mathcal{V} at constant conformal time η , the conserved charge, which is just the angular momentum, is

$$J_c = \int_{\mathcal{V}} a \delta T^{0k} \epsilon_{kcl} x^l \sqrt{\bar{g}_3} d^3 \vec{x}. \quad (3.26)$$

We emphasize here that the angular momentum obtained in Eq. (3.26), through the formalism of [39], coincides with the starting expression in [6, 7]. The latter obtained Eq. (3.26) by assuming that the hypersurface integral version of the Komar formula for angular momentum, Eq. (3.15), still holds even in the perturbed FRW case by simply replacing $T_{\mu\nu}$ with the perturbed energy momentum tensor.

We proceed with the calculation of the angular momentum, for a spherical volume with comoving radius x_0 enclosing some fluid. Adopting Cartesian coordinates for the background FRW spacetime, we have

$$\sqrt{\bar{g}_3} = a^3. \quad (3.27)$$

If we assume that the perturbation to the momentum flow is a gradient of some potential ψ , then the integral over the spherical volume is

$$\int_{\mathcal{V}} \epsilon^{kal} x_l \partial_k \psi d^3 \vec{x} = \oint_{\partial \mathcal{V}} \epsilon^{kal} x_0 n_l n_k \psi dS = 0. \quad (3.28)$$

It was pointed out by [5, 43] that one must consider the second-order contribution to angular momentum in the case of spherical volumes. The determinant of the spatial part of the metric, to first order in perturbations, is given by

$$g_3 \approx (a^3)^2 (1 + 6\Phi + 2\nabla^2 \gamma). \quad (3.29)$$

We take

$$\delta T_{0j} = \partial_j \psi \equiv \bar{\rho} (1 + \delta) a v_j, \quad (3.30)$$

where δ is the fluid density contrast, and v_j is a dimensionless velocity term, which arises from a potential, *i.e.*

$$v_j = -\partial_j \theta. \quad (3.31)$$

Then the nonvanishing part of the integral is

$$J_c \approx a \bar{\rho} a^4 \epsilon_{ijc} \int_{x < x_0} d^3 \vec{x} x^i v^j (\delta + 3\Phi + \nabla^2 \gamma). \quad (3.32)$$

Note that the integrand consists of products of two first-order quantities. Aside from the product of the density contrast and fluid velocity, which is present in [43] and [5], we also have the following contributions: the products of the fluid velocity and gravitational potential, and the fluid velocity and $\nabla^2 \gamma$.

To determine the evolution of the angular momentum, it is convenient to first expand the perturbations in terms of their Fourier modes. We can express the angular momentum as an integral over the momenta \vec{k} and \vec{k}' , and the integrand can be expressed as a product of a geometric form factor, associated with the spherical shape of the integration volume in comoving coordinates, and a product of the density and velocity potential. Defining

$$\hat{\psi}_k \equiv i \hat{k} \cdot \vec{v}_k = k \theta_k, \quad (3.33)$$

we have

$$\vec{J} = -a \, 4\pi \bar{\rho} R^4 x_0 \int d\Pi_k d\Pi_{k'} (\vec{k} \times \vec{k}') \delta_{\text{eff}}(\vec{k}) \frac{\hat{\psi}(\vec{k}')}{k'} \mathcal{F}(|\vec{k} + \vec{k}'|x_0), \quad (3.34)$$

where

$$\delta_{\text{eff}}(\vec{k}, \eta) \equiv \delta(\vec{k}, \eta) + 3\Phi(\vec{k}, \eta) - k^2 \gamma(\vec{k}, \eta), \quad (3.35)$$

$$R(\eta) = x_0 a(\eta), \quad d\Pi_k \equiv \frac{d^3 \vec{k}}{(2\pi)^3}, \quad \mathcal{F}(z) \equiv \frac{3z \cos z - (3 - z^2) \sin z}{z^5}. \quad (3.36)$$

The quantity R is the physical radius of the false vacuum bubble with comoving size x_0 , at conformal time η . Following [43], we subtract the contribution from the translational motion of the sphere's center of mass (CM). We find that the angular momentum about the CM is

$$\vec{J}_{\text{CM}}(\eta) = 4\pi \bar{\rho} R^5 \int d\Pi_k d\Pi_{k'} (\vec{k} \times \vec{k}') \delta_{\text{eff}}(\vec{k}, \eta) \quad (3.37)$$

$$\times \left[\mathcal{F}(|\vec{k} + \vec{k}'|x_0) - 3\mathcal{F}(kx_0)\mathcal{G}(k'x_0) \right] \frac{\hat{\psi}(\vec{k}', \eta)}{k'}, \quad (3.38)$$

where the function \mathcal{G} is defined as

$$\mathcal{G}(y) \equiv \frac{\sin y - y \cos y}{y^3}. \quad (3.39)$$

Since the density and velocity perturbations are seeded by initial Gaussian curvature perturbations, the conditional probability, $P(\vec{J}|x_0)$, of obtaining an angular momentum \vec{J} for any sphere with comoving radius x_0 is Gaussian with zero mean, and can be constructed entirely from the two-point function $\langle J^a J^b \rangle$. This transforms properly as a tensor under spatial rotations and can be shown to be diagonal, so we can write

$$P(\vec{J}|x_0, \eta) = \frac{3}{J_{\text{CM,rms}}^2(x_0, \eta) \sqrt{2\pi}} \exp \left[-\frac{3\vec{J}^2}{2J_{\text{CM,rms}}^2(x_0, \eta)} \right]. \quad (3.40)$$

A similar statement can be made about the spin parameter,

$$\vec{s} \equiv \frac{\vec{J}}{G_N M^2}. \quad (3.41)$$

For a spherical volume with physical radius R , the mass of the enclosed fluid f is $M = 4\pi/3 \bar{\rho}_f R^3$. An explicit expression for the RMS value of the CM angular momentum is given by

$$J_{\text{CM,rms}}^2 = \left(\frac{3}{4} A_s M R \right)^2 \tilde{x}_0^2 \mathcal{C}(\tilde{x}_0, x_0), \quad (3.42)$$

$$\mathcal{C}(\tilde{x}_0, x_0) \equiv A_s^{-2} \int_0^\infty dz \, z \int_0^\infty dz' \, z' \times \int_{-1}^1 dx \, (1-x^2) W^2(z, z'; \tilde{x}_0) \Delta_{\mathcal{R}}^2(k) \Delta_{\mathcal{R}}^2(k'), \quad (3.43)$$

$$W(z, z'; \tilde{x}_0) \equiv \frac{U_{\text{eff}}(k) U_\psi(k') (\mathcal{F}_{k+k'} - 3\mathcal{F}_k \mathcal{G}_{k'})}{z'} - (z \leftrightarrow z'), \quad (3.44)$$

where the integration variables z , z' , and x are

$$z \equiv \frac{1}{\sqrt{3}} \frac{k}{\mathcal{H}}, \quad z' \equiv \frac{1}{\sqrt{3}} \frac{k'}{\mathcal{H}}, \quad x \equiv \hat{k} \cdot \hat{k}'. \quad (3.45)$$

We have also introduced the rescaled form of the curvature power spectrum

$$\Delta_{\mathcal{R}}^2(k) \equiv \frac{k^3 P_{\mathcal{R}}(k)}{2\pi^2}. \quad (3.46)$$

The quantity $P_{\mathcal{R}}(k)$ is essentially the mean squared value of the curvature fluctuation \mathcal{R}_k , which should be thought of as a Gaussian random variable with zero mean. More precisely,

$$\langle \mathcal{R}_k \mathcal{R}_{k'} \rangle = (2\pi)^3 P_{\mathcal{R}}(k) \delta^{(3)}(\vec{k} - \vec{k}'), \quad (3.47)$$

with

$$P_{\mathcal{R}}(k) = \frac{2\pi^2}{k^3} A_s \left(\frac{k}{k_s} \right)^{n_s-1}, \quad (3.48)$$

where A_s is the amplitude of superhorizon curvature perturbations, k_s is the tilt scale, and n_s is the spectral index of scalar perturbations. The measured values are given by [44]:

$$A_s = (2.196 \pm 0.060) \times 10^{-9}, \quad (3.49)$$

$$k_s = 0.05 \text{ Mpc}^{-1} = 3.205 \times 10^{-31} \text{ eV}, \quad n_s = 0.9603 \pm 0.0073. \quad (3.50)$$

In Eq. (3.43) it is understood that, *e.g.* $\mathcal{F}_{k+k'} \equiv \mathcal{F}(|\vec{k} + \vec{k}'|x_0)$, $\mathcal{F}_k \equiv \mathcal{F}(kx_0)$ and $\mathcal{G}_k \equiv \mathcal{G}(kx_0)$. We have introduced the parameter,

$$\tilde{x}_0(\eta) \equiv \sqrt{3} \mathcal{H} x_0, \quad (3.51)$$

to refer to the size of the spherical volume, with comoving radius x_0 , relative to the size of the Hubble horizon, at conformal time η when the comoving Hubble parameter is \mathcal{H} . To factor out the amplitude of the curvature perturbation, which carries the statistical information about the perturbations, we have introduced the transfer functions

$$U_{Q_I}(k) \equiv \frac{Q_I(k)}{\mathcal{R}_k}, \quad (3.52)$$

where Q_I is any perturbation; for example, $U_\psi(k) \equiv \hat{\psi}_k/\mathcal{R}_k$, $U_{\text{eff}}(k) \equiv \delta_{\text{eff}}(k)/\mathcal{R}_k$.

3.3 Spin of primordial black holes

Our calculation of the angular momentum and spin of false vacuum remnants is motivated by the desire to determine the spin of PBHs formed by the direct collapse of FV bubbles or by the collapse of Fermi balls. On the other hand, the spin of PBHs from cosmological perturbations has been discussed extensively in the literature, mainly in Refs. [5–7], in the usual context of PBH formation through the collapse of overdensities. These sizable density perturbations in the cosmological fluid are seeded by rare peaks in the curvature power spectrum. Such enhancements in the power spectrum may be realized in certain inflationary models [45–47]. However, there seems to be an apparent disagreement between the two main approaches to this mechanism. Reference [6] argued that it is appropriate to consider ellipsoidal volumes in describing overdensities. This follows from an earlier work by [16] in which the overdensities are expanded to quadratic order about the peak and the overdensity within the volume is required to be at least a certain fraction of the peak value, which is one of the criteria to ensure the collapse into PBHs; then, in general, the boundary of this volume is triaxial. The relevant phase space of triaxial configurations and velocity shear has 16 dimensions, where the phase space variables are: overdensity; first and second derivatives of the overdensity; and the first derivative of the velocity field. The joint probability distribution over this configuration space is essentially Gaussian [48], where the covariance matrix, which contains the two point correlators of the phase space variables, is ultimately determined by the fluid transfer functions and curvature perturbations. In choosing the gauge, they considered constant mean curvature slicing [17, 49, 50], which is equivalent to the uniform Hubble gauge, and worked in the subhorizon limit for the fluid perturbations. By considering ellipsoidal volumes, [6] showed that, starting from the Komar expression, angular momentum is a quantity that is *first order* in perturbations.

In contrast, the authors of Ref. [5] considered spherical volumes in their PBH spin calculation, which they have justified by referring to [48]. Firstly, they assumed that curvature perturbations ζ have rare high peaks in position space. Once these perturbations enter the horizon, they collapse into PBHs. In position space, one can construct contours of constant curvature, as shown in Figure 1 of Ref. [5]. The ellipticity of those contours is proportional to $\zeta_{\text{rms}}/\zeta_0$, where ζ_0 is the amplitude of the peak. Sending $\zeta_{\text{rms}} \rightarrow 0$ brings the ellipticity to zero. The angular momentum is calculated using Eq. (3.10), at a time when the PBH has already formed. It was argued, in a manner similar to Eq. (3.28), that the first-order contribution to the angular momentum is zero for a spherical volume, and thus the leading nonvanishing contribution is at *second order* in perturbations. The size of the integration volume is chosen carefully: the 3-volume around the PBH must be sufficiently large such that the spacetime geometry generated by the PBH is close to being Minkowski, but small enough that it does not see the curvature due to Hubble. These criteria can be easily realized at late times, but still during the radiation dominated era of the Universe, where the Hubble horizon has grown to a larger size. They then calculated the flux of angular momentum from acoustic waves through this 3-volume, and identified it with the torque on the PBH. Because they were interested in the initial spin of PBHs, they extrapolated their result to early times. It is worth noting that they worked in the Newtonian gauge, used the subhorizon limit for the evolution of perturbations, and considered an enhanced power spectrum with a narrow Gaussian peak.

3.4 Angular momentum due to uniform pressure

One may wonder about the angular momentum on a closed surface due to the torque generated by a uniform fluid pressure. A simple argument can be formulated to demonstrate that the result is zero. We start by considering a generic, smooth surface, defined parametrically as

$$\vec{r} = \vec{\xi}(u, v). \quad (3.53)$$

The area element on the surface is

$$d\vec{A} = \partial_u \vec{\xi} \times \partial_v \vec{\xi} \, du dv, \quad (3.54)$$

where $\partial_u \equiv \hat{u} \cdot \vec{\nabla}$, $\partial_v \equiv \hat{v} \cdot \vec{\nabla}$. If $\Delta \vec{\xi} \equiv \vec{\xi} - \langle \vec{r}_c \rangle$ is the position vector on the surface, relative to the center of mass position $\langle \vec{r}_c \rangle$ of the bulk fluid enclosed by the surface, then the infinitesimal torque is then given by

$$d\vec{\tau}^i = p \left[\Delta \vec{\xi} \times \left(\partial_u \vec{\xi} \times \partial_v \vec{\xi} \right) \right]^i \, du dv \quad (3.55)$$

$$= \frac{p}{2} \left[\partial_v \left(\Delta \vec{\xi} \right)^2 \partial_u \Delta \xi^i - \partial_u \left(\Delta \vec{\xi} \right)^2 \partial_v \Delta \xi^i \right] \, du dv. \quad (3.56)$$

Here we have taken p to be the uniform pressure on the surface. The above expression can be shown to be a total derivative, *i.e.*

$$d\vec{\tau}^i = \frac{p}{2} \vec{\nabla} \times \left[\Delta \xi^i \vec{\nabla} \left(\Delta \vec{\xi} \right)^2 \right] \cdot d\vec{A}. \quad (3.57)$$

One can use Stokes' theorem to integrate the torque over the closed surface, and show that the result is zero.

4 Evolution of cosmological perturbations

The angular momentum of a spherical volume containing several fluid components can be computed once the perturbations on each fluid component and the gravitational potentials Φ and γ are known. We identify the periods in cosmological history that are crucial for us: the conformal time $\eta = \eta_0 \simeq 0$ at which all perturbations are superhorizon, the critical point $\eta = \eta_c$, and the onset of percolation $\eta = \eta_*$. In what follows, quantities evaluated at the percolation time are indicated with a subscript $*$. Here we aim to calculate only the perturbations, and eventually the angular momentum, during $[0, \eta_c]$ and $[\eta_c, \eta_*]$. The subsequent evolution, which will result in either the direct collapse to a PBH or the formation of a FB before collapsing into a PBH, is described by different dynamics beyond the scope of our study.

Following Ref. [21], and working in the UHG, we can track the evolutions of δ , $\hat{\psi}$, and Φ . For a fluid component f , the equation of state and sound speeds, defined as

$$w_f \equiv \frac{p_f}{\rho_f}, \quad c_{s,f}^2 \equiv \left(\frac{\partial \rho_f}{\partial p_f} \right)_s = \frac{d\rho_f/dT}{dp_f/dT}, \quad (4.1)$$

must be known a priori. The zeroth order continuity equation gives

$$\sum_f [\rho'_f + 3\mathcal{H}(1 + w_f)\rho_f] = 0, \quad (4.2)$$

while the first order perturbations evolve via

$$\frac{\delta'_f}{\mathcal{H}} - \frac{k}{\mathcal{H}} \hat{\psi}_f + 3(1 + w_f) \Psi_k + 3(c_{s,f}^2 - w_f) \delta_f = 0, \quad (4.3)$$

$$\frac{\hat{\psi}'_f}{\mathcal{H}} + (1 - 3w_f) \hat{\psi}_f + c_{s,f}^2 \frac{k}{\mathcal{H}} \delta_f + (1 + w_f) \frac{k}{\mathcal{H}} \Psi_k = 0. \quad (4.4)$$

Note that in Eqs. (4.2)-(4.4), the prime denotes differentiation with respect to the conformal time η . In Fourier space, the analog of the Poisson equation which gives the gravitational potential Ψ_k is

$$\left[\left(\frac{k}{\mathcal{H}} \right)^2 + \frac{9}{2}(1 + w) \right] \Psi_k + \frac{3}{2}(1 + 3c_s^2) \delta = 0, \quad (4.5)$$

where

$$w \equiv \frac{\sum_f w_f \rho_f}{\sum_f \rho_f}, \quad c_s^2 \equiv \frac{\sum_f c_{s,f}^2 \rho'_f}{\sum_f \rho'_f}, \quad \delta \equiv \frac{\sum_f \delta_f \rho_f}{\sum_f \rho_f}. \quad (4.6)$$

The gravitational potential Φ can be obtained from the linearized Einstein field equations in the UHG via

$$\nabla^2 \Phi = -4\pi G_N a^2 \sum_f \rho_f \delta_f = -\frac{3}{2} \mathcal{H}^2 \frac{\sum_f \rho_f \delta_f}{\sum_f \rho_f}, \quad \mathcal{H} \equiv \frac{a'}{a}, \quad (4.7)$$

where we used the Friedmann equation in the last equation. Meanwhile, the metric perturbation γ in Fourier space can be obtained from

$$(-k^2 \gamma_k)' = \frac{9}{2} \frac{\mathcal{H}^2}{k} \frac{\sum_f \rho_f \hat{\psi}_f}{\sum_f \rho_f}, \quad (4.8)$$

and we couple Eq. (4.8) with Eqs. (4.3) and (4.4). We note that if the perturbations δ_f and θ_f across fluids are of the same order, then the fluid component that contributes dominantly to the total background energy density is expected to contribute the most to Φ and γ . Typically it is assumed that the dominant fluid component is the SM plasma, but this condition may be relaxed.

4.1 Evolution of perturbations: η_0 to η_c

In the radiation dominated era of the early Universe, we have

$$\mathcal{H} = \frac{1}{\eta}, \quad 0 < \eta < \eta_c. \quad (4.9)$$

Note that the SM fluid component has $w = c_s^2 = 1/3$. On the other hand, the χ and ϕ fluid components constitute a tightly coupled system and should be treated as a single fluid component, similar to the baryon-photon fluid. In the following, we refer to this fluid as the dark plasma $D = \chi + \phi$. Before the onset of the FOPT, the dark plasma still has $w = c_s^2 = 1/3$. Noting that the SM plasma has a temperature T_{SM} that is assumed to be

much larger than the dark plasma temperature T , we have $\rho_{\text{SM}} \gg \rho_{\text{D}}$. Thus, $\delta \approx \delta_{\text{SM}}$, so that perturbations in the SM plasma mainly dictate the evolution of Ψ_k . Then

$$\Psi_k \simeq -\frac{\delta_{\text{SM}}}{2 + (k\eta)^2/3}. \quad (4.10)$$

The evolution of the SM radiation fluid perturbations are given by

$$\delta'_{\text{SM}} = k\hat{\psi}_{\text{SM}} - \frac{4}{\eta}\Psi_k, \quad (4.11)$$

$$\hat{\psi}'_{\text{SM}} = -\frac{k}{3}\delta_{\text{SM}} - \frac{4}{3}k\Psi_k. \quad (4.12)$$

The initial conditions are set by the primordial curvature perturbation $\mathcal{R}_k(0)$ associated with the comoving wavenumber k , when modes are superhorizon. In the case where the background Hubble evolution is determined solely by a component with constant w , and with a constant sound speed $c_s^2 = w$, the evolution equations for the perturbations admit exact solutions. For the SM plasma with $w = c_s^2 = 1/3$, one can show that the density and velocity perturbations in the UHG are [51]

$$\delta_{\text{SM}}(k, \eta) = 2\mathcal{R}_k(0)z^2T_\delta(z), \quad \hat{\psi}_{\text{SM}}(k, \eta) = \frac{2\mathcal{R}_k(0)}{3\sqrt{3}}z^3T_{\hat{\psi}}(z), \quad (4.13)$$

where

$$T_\delta(z) \equiv \frac{2(2\sin z - z\cos z)}{z(2+z^2)}, \quad T_{\hat{\psi}}(z) \equiv \frac{6[2z\cos z + (z^2-2)\sin z]}{z^3(2+z^2)}, \quad z \equiv \frac{k\eta}{\sqrt{3}}. \quad (4.14)$$

It also follows that

$$\Phi_k \simeq \frac{1}{2z^2}\delta_{\text{SM}}(k) = \mathcal{R}_k(0)T_\delta(z). \quad (4.15)$$

Observe that the perturbations in the UHG, given by Eqs. (4.13) and (4.15) are nonsingular in the superhorizon regime $z \rightarrow 0$, and this is another advantage of adopting the UHG, as pointed out by, *e.g.* [40] and [21]. In fact, as shown in the left panel of Fig. 2, the transfer functions are close to unity at early times, *i.e.* when the modes are superhorizon. As for $\nabla^2\gamma$ in Fourier space, we can obtain it by integrating the ordinary differential equation (ODE),

$$\frac{d}{dz}(-k^2\gamma_k) = \frac{3\sqrt{3}}{2}\frac{\hat{\psi}_{\text{SM}}(z)}{z^2}, \quad (4.16)$$

where we set the initial condition to be such that $-k^2\gamma_k = 0$ at $z = 0$. When the mode enters the horizon, *i.e.* when $k \sim \mathcal{H} = 1/\eta$, the perturbations start to oscillate as they feel the presence of the radiation fluid with a nonzero sound speed. One can similarly write down the evolution equations for δ_{D} and $\hat{\psi}_{\text{D}}$, and find that

$$\delta_{\text{D}} \simeq \delta_{\text{SM}}, \quad \hat{\psi}_{\text{D}} \simeq \hat{\psi}_{\text{SM}}. \quad (4.17)$$

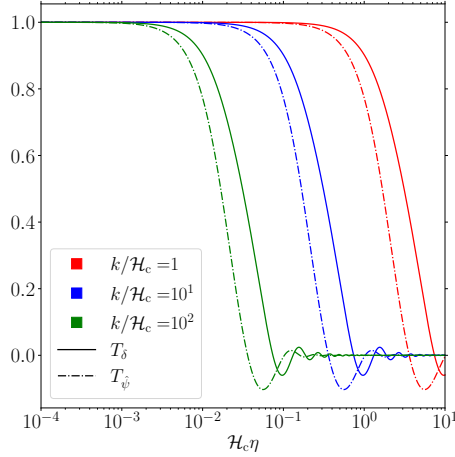


Figure 2. The transfer functions T_δ and T_ψ in a radiation dominated background cosmology, for different perturbation modes.

4.2 Evolution of perturbations: η_c to η_*

4.2.1 Background evolution

From the critical temperature up to percolation, the usual cosmological evolution of the Universe is modified by first-order phase transition (FOPT) dynamics. The FOPT is triggered mainly by the effective potential given in Eq. (2.2) developing a nonzero vacuum expectation value.

During the FOPT, the equation of state of the dark fluid is modified, which will affect the evolution of the density and velocity perturbations in the dark sector. This requires us to first track the background cosmological evolution during the FOPT. Furthermore, tracking the background cosmological evolution will allow us to determine relevant physical quantities at the percolation time. The total energy density that drives the cosmological expansion is given by

$$\rho = \rho_{\text{SM}}(t) + \rho_{\text{D}}(t), \quad \rho_{\text{D}}(t) \equiv \rho_{\text{FV}}(T(t)) - [1 - F(t)] \Delta\rho(t), \quad (4.18)$$

where $F(t)$ is the fraction of the Universe in the false vacuum. We can write the energy density of the SM radiation component as

$$\rho_{\text{SM}} = \rho_{\text{SM},c} a^{-4}, \quad \rho_{\text{SM},c} = \frac{\pi^2}{30} g_{\rho,\text{SM},c} T_{\text{SM},c}^4. \quad (4.19)$$

The value of $g_{\rho,\text{SM},c}$ is taken from [52]. The reduced Hubble parameter, which is obtained by normalizing the Hubble parameter relative to its value at the critical temperature, is given by

$$h^2(t) \equiv \frac{H^2(t)}{H^2(t_c)} = \frac{\rho_{\text{SM}} + \rho_{\text{FV}} - (1 - F)\Delta\rho}{\rho_{\text{SM},c} + \rho_{\text{FV},c}}. \quad (4.20)$$

Assuming that the bubbles expand as in a *detonation* process, the shock front trails behind the expanding bubble wall, so that reheating occurs only in the true vacuum regions. Only

when the bubbles collide is there a sudden release of latent heat. Since we do not model the dynamics of bubble collisions, we simply take

$$\dot{T} = -HT, \quad (4.21)$$

which is consistent with the continuity equation in the period before the latent heat is suddenly released. As for the false vacuum fraction $F(t)$, it can be obtained by knowing the nucleation rate $\Gamma(T)$, the bubble wall velocity v_w , and the scale factor for all t' such that $t_c \leq t' \leq t$. Then

$$-\ln F(t) = \frac{4\pi}{3} \int_{t_c}^t dt' \Gamma(T(t')) a^3(t') r^3(t, t'), \quad r(t, t') \equiv \int_{t'}^t dt'' \frac{v_w(t'')}{a(t'')}. \quad (4.22)$$

The wall velocity is as an important ingredient in tracking the false vacuum fraction. In particular, earlier work by [24, 53, 54] incorporated the evolution of the bubble wall velocity, where reheating effects in the case of deflagrations will slow down the advancing bubble wall. Recent work by, *e.g.* [55, 56], provided prescriptions to obtain the bubble wall velocity in a model-independent manner. Here we take a simplified approach, following Ref. [57], where

$$v_w = 1 - \left(\frac{T}{T_c} \right)^k, \quad k = 8. \quad (4.23)$$

We have checked that quantities that do not explicitly depend on the wall velocity, such as the percolation temperature and inverse FOPT duration, marginally depend on k . However, the spin of FV bubbles has a strong dependence on v_w . As we remarked in Section 2, the nucleation rate depends mainly on the particle physics model. The exact connection lies in the following expression

$$\Gamma(T) = T^4 \left[\frac{S_3(T)}{2\pi T} \right]^{3/2} \exp \left[-\frac{S_3(T)}{T} \right], \quad (4.24)$$

where $S_3(T)$ is the bounce action associated with the scalar field configuration that satisfies the equation of motion. In the case of quartic effective potentials for a single real scalar field, a semianalytic expression has been formulated in Ref. [58], which we adopt in this work. For our effective potential, we take S_3 to be

$$S_3(T) \equiv \frac{\pi a(T)}{\bar{\lambda}^{3/2}} \frac{8\sqrt{2}}{81} [2 - \delta_3(T)]^{-2} \sqrt{\frac{\delta_3(T)}{2}} [\beta_1 \delta_3(T) + \beta_2 \delta_3^2(T) + \beta_3 \delta_3^3(T)], \quad (4.25)$$

$$\beta_1 = 8.2938, \quad \beta_2 = -5.5330, \quad \beta_3 = 0.8180, \quad (4.26)$$

where

$$\delta_3(T) \equiv \frac{8\bar{\lambda}b(T)}{a^2(T)}, \quad \bar{\lambda} \equiv \frac{\lambda}{4}, \quad a(T) = AT + C, \quad b(T) \equiv D(T^2 - T_0^2), \quad D > 0. \quad (4.27)$$

We can now formulate the system of coupled first order ODEs which describe the background evolution in the false vacuum during the FOPT. The ODEs track $x \equiv H_c(t - t_c)$, $y \equiv T/T_c$, F , the derivatives of F , and $\tilde{\eta} \equiv \mathcal{H}_c(\eta - \eta_c)$. We set $a = 1$ at the critical point. This then implies

that $H_c = \mathcal{H}_c$. Taking the scale factor a to be the independent variable, one can show that

$$\frac{dx}{da} = \frac{1}{ah}, \quad (4.28)$$

$$\frac{dy}{da} = -\frac{y}{a}, \quad (4.29)$$

$$\frac{d(\ln F)}{da} = \frac{g_1}{a} v_w \frac{1}{ah}, \quad (4.30)$$

$$\frac{dg_{i+1}}{da} = \frac{g_i}{a} v_w \frac{1}{ah}, \quad 1 \leq i \leq 2 \quad (4.31)$$

$$\frac{dg_3}{da} = -8\pi a^3 \frac{\Gamma(T_c y)}{H_c^4} \frac{1}{ah}, \quad (4.32)$$

$$\frac{d\tilde{\eta}}{da} = \frac{1}{a^2 h}, \quad (4.33)$$

where

$$g_n(t) \equiv -\frac{4\pi}{3} \frac{3!}{(3-n)!} H_c^{4-n} \int_{t_c}^t dt' \frac{\Gamma(T(t'))}{H_c^4} a^3(t') r^{3-n}(t, t'). \quad (4.34)$$

The g_n s are dimensionless quantities that are related to the derivatives of $\ln F$, and can also be defined recursively via Eq. (4.31). A similar system of ODEs, in particular that converts the integro-differential equation into a system of ODEs, was obtained in Ref. [59] and recently in Ref. [60]. Note that our system of ODEs has one less equation than Ref. [60], if we do not include Eq. (4.33) in the counting, which only tracks the elapsed conformal time from the critical point in units of H_c . The initial conditions are

$$x = 0, \quad y = 1, \quad F = 1, \quad g_i = 0, \quad (4.35)$$

for $a = 1$. As for the temperature of the SM sector, we take it to be

$$T_{\text{SM}} \simeq \frac{T_{\text{SM},c}}{a} \simeq \frac{T_c}{a} \frac{1}{r_{T,c}}, \quad (4.36)$$

where $r_{T,c}$ is the dark to SM temperature ratio at the critical point. Finally, we check that the physical volume in the false vacuum regions is decreasing, at least at the percolation time. This can be expressed as [61, 62]

$$\frac{d}{dt}(a^3 F) = HF a^3 \left[3 + \frac{1}{H} \frac{d(\ln F)}{dt} \right] \quad (4.37)$$

$$= HF a^3 \left(3 + \frac{g_3 v_w}{ah} \right) < 0. \quad (4.38)$$

For illustration purposes, in Fig. 3 and in the following figures, we feature two specific FOPT scenarios: BP-2 and BP-7 from Table 1. For each case, the evolution of the temperature (solid) and false vacuum fraction (dashed) versus the rescaled elapsed conformal time $H_c(\eta - \eta_c)$, are shown in the top row plots. The labeling is based on Table 1, where we list the benchmark FOPT scenarios of interest. We mark the moment of percolation with a vertical dashed line. In both cases, we have taken $r_{T,c} = 0.4$. For these two cases, the percolation

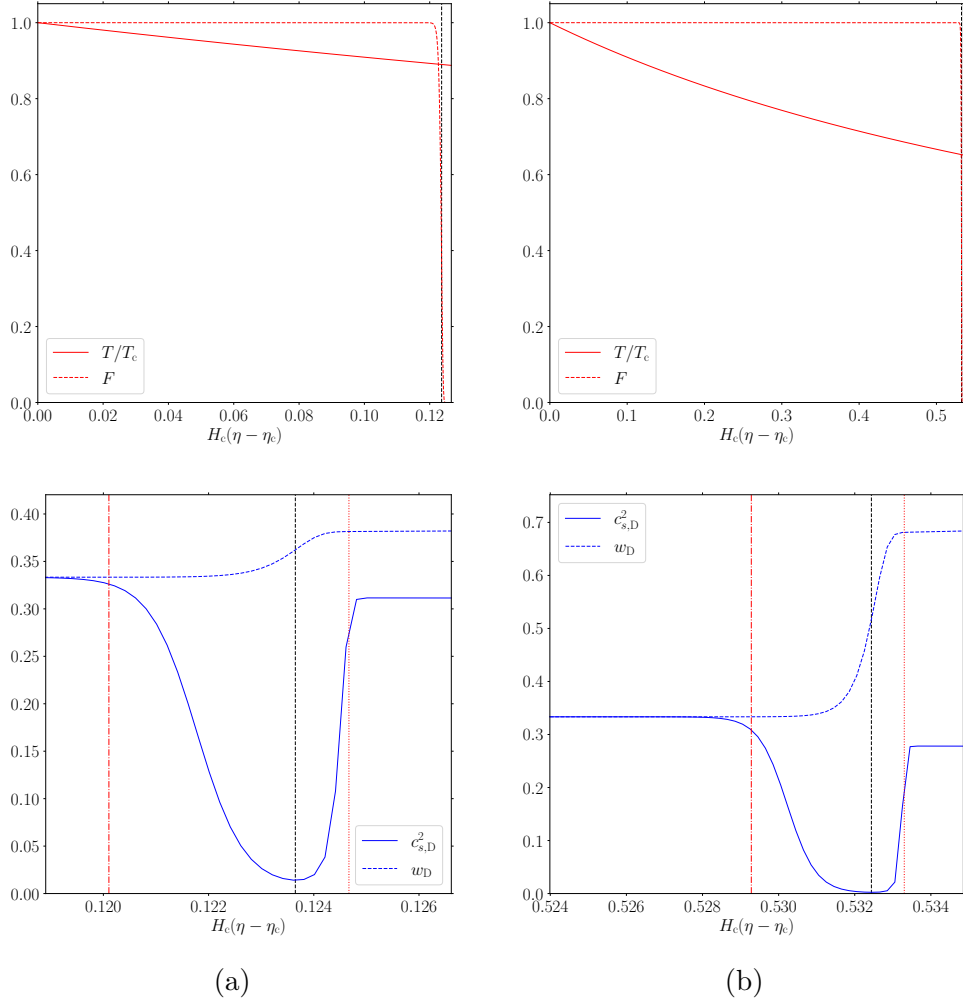


Figure 3. Evolution of the temperature and FV fraction (top row), and of $c_{s,D}^2$ and w_D (bottom), for BP-2 (column a) and BP-7 (column b). The vertical black dashed lines indicate the percolation temperature in all panels, while the vertical dot-dashed and dotted lines respectively indicate $\tilde{\eta}_i$ and $\tilde{\eta}_f$ in the bottom panels.

temperatures are such that $T_*/T_c < 0.9$, and the phase transition strength α_* is at least 10^{-4} . Here we define α_* as

$$\alpha_* \equiv \frac{1}{\rho_{R,\text{tot}}} \left(1 - \frac{T}{4} \frac{d}{dT} \right) \Delta V(T) \Big|_{T=T_*}, \quad \rho_{R,\text{tot}}(T_*) = \frac{\pi^2}{30} T_*^4 \left[g_\rho + \frac{g_{\rho,\text{SM}}(T_*)}{r_{T,c}^4} \right]. \quad (4.39)$$

The difference in the conformal time elapsed, from the critical point up to the percolation time, for these two cases can be estimated by first noting that $T \propto 1/a$ and $a \propto \eta$ in the radiation-dominated era. Then

$$H_c(\eta_* - \eta_c) \approx \frac{1 - T_*/T_c}{T_*/T_c}. \quad (4.40)$$

From the above estimate, a lower percolation temperature implies a longer conformal time duration between the critical point and percolation. The percolation temperature, in turn,

	BP-1	BP-2	BP-3	BP-4	BP-5	BP-6	BP-7	BP-8
A	10^{-1}	10^{-1}	10^{-2}	10^{-2}	10^{-2}	10^{-2}	10^{-3}	10^{-4}
x_C	1.0365×10^{-2}	1.0365×10^{-2}	2.251×10^{-3}	2.251×10^{-3}	2.251×10^{-3}	1.4989×10^{-4}	2.1463×10^{-5}	1.6172×10^{-5}
λ	0.1836	0.1836	1.4043×10^{-2}	1.4043×10^{-2}	1.4043×10^{-2}	8.522×10^{-3}	3.9556×10^{-4}	1.836×10^{-5}
L_c/T_c^4	9.0569×10^{-2}	9.0569×10^{-2}	5.0496×10^{-2}	5.0496×10^{-2}	5.0496×10^{-2}	4.8887×10^{-2}	9.0569×10^{-2}	0.8
T_c (MeV)	10^5	10	10^5	10	1	10	10^3	10^{-2}
$r_{T,c}$	0.4	0.4	0.4	0.1	0.4	0.4	0.4	0.1
T_* (MeV)	8.7132×10^4	8.8996	8.0128×10^4	8.1911	0.8299	6.6853	6.5256×10^2	8.788×10^{-3}
$\sqrt{3}H_*R_*$	1.1926×10^{-3}	6.9296×10^{-4}	1.9432×10^{-3}	1.4573×10^{-3}	1.2045×10^{-3}	2.1579×10^{-3}	6.5936×10^{-4}	5.6272×10^{-5}
M_*/M_\odot	3.2916×10^{-19}	1.6059×10^{-10}	1.7103×10^{-18}	2.4759×10^{-13}	1.1649×10^{-7}	8.2059×10^{-9}	1.2081×10^{-15}	5.1961×10^{-11}
α_*	2.7930×10^{-5}	2.3249×10^{-4}	2.5184×10^{-5}	5.7671×10^{-7}	2.1285×10^{-4}	3.1267×10^{-4}	1.0988×10^{-4}	4.8694×10^{-5}
$(\beta/H)_*$	1.4602×10^3	2.3087×10^3	1.1229×10^3	1.4446×10^3	1.7025×10^3	1.1835×10^3	3.9481×10^3	5.3696×10^4
$v_{w,*}$	0.6678	0.6065	0.8301	0.7974	0.7751	0.9601	0.9671	0.6443
$s_{\text{rms},*}/(v_{\text{eff},*}/A_s)$	9.1707	3.0934	3.4005	2.5764×10^2	0.901	0.3341	2.7841×10^1	8.6758×10^4
$\tilde{\eta}_* - \tilde{\eta}_i$	6.8894×10^{-3}	4.563×10^{-3}	9.7022×10^{-3}	7.6396×10^{-3}	6.531×10^{-3}	1.1398×10^{-2}	4.019×10^{-3}	7.9014×10^3
$c_{s,D*}^2$	1.9829×10^{-2}	1.4258×10^{-2}	3.2436×10^{-2}	2.8191×10^{-2}	2.5533×10^{-2}	1.6212×10^{-2}	2.4072×10^{-3}	4.1637×10^{-4}
$\tilde{\eta}_*$	0.1477	0.1236	0.248	0.2208	0.205	0.4958	0.5324	0.1379
C_*	2.866×10^1	4.5227×10^2	3.9446	3.7088×10^1	1.3023×10^2	1.8728	1.2146×10^1	1.0821×10^5
$v_{\text{eff},*}/A_s$	4.7884×10^{-3}	1.1053×10^{-2}	2.8945×10^{-3}	6.6561×10^{-3}	1.0309×10^{-2}	2.2148×10^{-3}	1.7235×10^{-3}	1.3883×10^{-2}
$s_{\text{rms},*}$	4.3913×10^{-2}	3.419×10^{-2}	9.8429×10^{-3}	1.7149	9.2887×10^{-3}	7.4004×10^{-4}	4.7984×10^{-2}	1.2045×10^3

Table 1. Selection of benchmark points from our scan.

can be approximated by [63]

$$-\ln F(t) \approx \frac{4\pi}{3} v_w^3 \int_{t_c}^t dt' \Gamma_* \exp[\beta_*(t' - t_*)] (t - t')^3 \approx 8\pi \frac{v_w^3}{\beta^4(t)} \Gamma(t), \quad (4.41)$$

where

$$\frac{\beta(t)}{H} = \frac{1}{H} \dot{\Gamma} \simeq T \frac{d}{dT} \left(\frac{S_3}{T} \right) \quad (4.42)$$

is the inverse time scale of the FOPT at time t . In the last line, we assume that the nucleation rate increases monotonically with time, the scale factor is approximately constant, and $\beta_*(t - t_c) \gg 1$. In the final step, we replaced Γ_* with $\Gamma(t)$, and β_* with $\beta(t)$. Then

$$1 \approx \frac{8\pi}{3} v_{w,*}^3 \frac{\Gamma_*}{\beta_*^4} \Rightarrow \exp \left[\frac{S_3(T_*)}{T_*} \right] \approx \frac{8\pi}{3} \left[\frac{S_3(T_*)}{T_*} \right]^{3/2} \frac{v_w^3}{(\beta_*/H_*)^4} \left(\frac{T_*}{H_*} \right)^4. \quad (4.43)$$

Typically, the bounce action at percolation for an FOPT with $T_c = 10$ MeV and $r_{T,c} = 0.4$ is $S_3/T \sim 150$. In Fig. 4 we plot S_3/T as solid curves, where we feature BP-2 (red) and BP-7 (blue). It can be seen that the typical value $(S_3/T) \sim 150$ corresponds to a higher percolation temperature for BP-2 compared to BP-7. For reference, we indicated the actual percolation temperatures as vertical dot dashed lines. Note that the actual values of $S_3(T_*)/T_*$ for BP-2 and BP-7 are, respectively, 155.78 and 133.86. The difference can be mainly attributed to the fact that these benchmark points have different critical temperatures. In fact, based on the estimate in Eq. (4.43), the respective values of $S_3(T_*)/T_*$ for BP-2 and BP-7 are expected to differ by $4 \ln[(1 \text{ GeV}/10 \text{ MeV})] \simeq 18$. In order to account for the presence of the FV and TV, the thermodynamic properties of the dark fluid are determined by the average of the FV and TV contributions, weighted by the respective volume fractions, *i.e.*

$$p_D = F p_{\text{FV}} + (1 - F) p_{\text{TV}}, \quad s_D = F s_{\text{FV}} + (1 - F) s_{\text{TV}}, \quad \rho_D = F \rho_{\text{FV}} + (1 - F) \rho_{\text{TV}}. \quad (4.44)$$

We comment that the above prescription, which uses volume fractions as weights to account for the contribution of each phase, is valid over sufficiently large scales where FV and TV

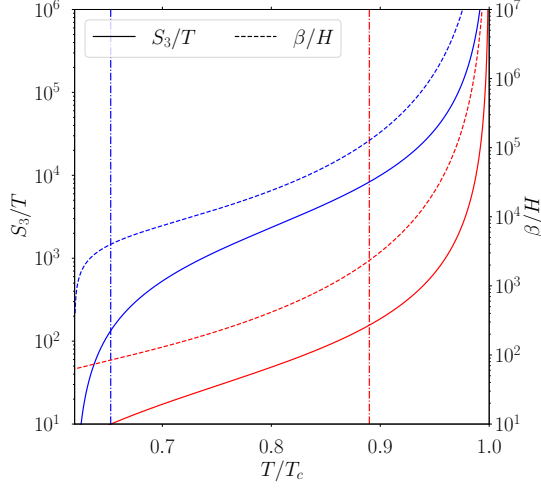


Figure 4. S_3/T and β/H , for BP-2 (red) and BP-7 (blue). The vertical dot-dashed lines indicate the percolation temperature for each benchmark.

features are indistinguishable. Meanwhile, the dark sector equation of state, and the sound speed are then respectively given by

$$w_D = \frac{p_D}{\rho_D}, \quad c_{s,D}^2 = \frac{dp_D/dt}{d\rho_D/dt} = \frac{s_D - \left(\frac{\dot{F}}{H}\right) \frac{\Delta p}{T}}{T \frac{\partial s_D}{\partial T} - \left(\frac{\dot{F}}{H}\right) \frac{\Delta \rho}{T}} = \frac{1}{3} \left[\frac{1 - (1-F) \frac{T \Delta s}{4 p_{FV}}}{1 - \frac{\dot{F}}{H} \frac{\Delta \rho}{4 \rho_{FV}}} \right]. \quad (4.45)$$

Note that in the limit where the system is predominantly in one of the vacuum configurations, $\dot{F}/H \rightarrow 0$, so that

$$w_D \rightarrow \frac{p_i}{\rho_i}, \quad c_{s,D}^2 \rightarrow c_{s,i}^2 \equiv \left(\frac{d \ln s_i}{d \ln T} \right)^{-1}, \quad i = FV, TV. \quad (4.46)$$

We emphasize that $c_{s,i}^2$ in this limit refers to the sound speed in the FV or the TV, when each is taken in isolation. This is the sound speed that has been computed in *e.g.* [25, 27]. However, during the phase transition, the sound speed $c_{s,D}^2$ in the dark plasma may deviate from the value suggested by $c_{s,FV}^2$ or $c_{s,TV}^2$. For example, if the false vacuum fraction decreases sharply, the denominator in Eq. (4.45) can be large so that $c_{s,D}^2$ can be close to zero. A similar situation occurs in the physical system considered in Ref. [21], where the system undergoes prolonged phase coexistence at $T \simeq T_c$, keeping the pressure constant, which leads to a zero sound speed in the long-wavelength limit. On the other hand, Ref. [27] mentioned in a footnote that the sound speed does not vanish at the critical point, which is contrary to the result in Ref. [21]. This is not very surprising, since the former considered the sound speeds in each phase taken in isolation, *i.e.* $c_{s,FV}^2$ and $c_{s,TV}^2$. For the sake of clarity, in Table 2 we explicitly define those quantities, such as the equation of state and sound speed squared, that refer to: the different phases in the dark sector; the weighted average over phases in the dark sector; the weighted average over fluids in the cosmological system.

Quantity	Description
w_{FV}	False vacuum equation of state in the dark sector
w_{TV}	True vacuum equation of state in the dark sector
w_{D}	Dark sector equation of state, weighted over the false and true vacua
w_{SM}	Visible sector equation of state
w	Average equation of state, weighted over the dark and visible sectors
$c_{s,\text{FV}}^2$	False vacuum sound speed squared in the dark sector; always equal to 1/3
$c_{s,\text{TV}}^2$	False vacuum sound speed squared in the dark sector; not necessarily 1/3
$c_{s,\text{D}}^2$	Dark sector sound speed squared, weighted over the false and true vacua
$c_{s,\text{SM}}^2$	Visible sector sound speed squared
c_s^2	Average sound speed squared, weighted over the dark and visible sectors
$\delta_{\text{D}}, \hat{\psi}_{\text{D}}$	Density and velocity contrasts in the dark sector, respectively
$\delta_{\text{SM}}, \hat{\psi}_{\text{SM}}$	Density and velocity contrasts in the visible sector, respectively
δ	Density contrast, weighted over the dark and visible sectors
δ_{eff}	Effective density contrast in the angular momentum, Eq. (3.32)

Table 2. Summary of the main quantities relevant in tracking the background cosmology and perturbations.

Like the background evolution history, the evolution of the FV equation of state and the sound speed qualitatively differ between the two benchmark cases in Fig. 3. Based off Eq. (2.21), the sound speed for BP-2, with a higher percolation temperature, plateaus to a larger $c_{s,\text{D}}^2 \simeq c_{s,\text{TV}}^2$ than BP-7, shown as solid curves in the bottom row of Fig. 3. On the other hand, we both see dip features in the $c_{s,\text{D}}^2$ evolution. We can estimate the duration $\eta_f - \eta_i$ when the dark plasma sound speed deviates significantly from either $c_{s,\text{FV}}^2$ and $c_{s,\text{TV}}^2$ as follows. From Eq. (4.41) the rate of change in FV fraction is

$$\frac{-\dot{F}}{HF} \approx 4\pi v_{\text{w}}^3 \frac{1}{H} \int_{t_c}^t dt' \Gamma_* \exp[\beta_*(t' - t_*)] (t - t')^3 \approx 8\pi \frac{v_{\text{w}}^3}{\beta^3} \frac{\Gamma(t)}{H(t)}. \quad (4.47)$$

Since $\dot{T} = -HT$, the temperature decreases monotonically with time, and we take $T_i = T(\eta_i)$ to be the temperature when $\dot{F} = -HF$, *i.e.* the relative decrease in the FV fraction within a Hubble time is order unity. Then

$$8\pi \frac{v_{\text{w}}^3(T_i)}{(\beta/H)^3(T_i)} \frac{\Gamma(T_i)}{H^4(T_i)} = 1 \Rightarrow 8\pi \frac{v_{\text{w}}^3(T_i)}{(\beta/H)^3(T_i)} \frac{\Gamma(T_i)}{H_c^4} \left(\frac{T_c}{T_i}\right)^8 \simeq 1. \quad (4.48)$$

In the last equation, we approximated the Hubble parameter as

$$H \approx H_c \left(\frac{\rho_{\text{SM}}}{\rho_{\text{SM},c}}\right)^{1/2} \approx H_c \left(\frac{T_{\text{SM}}}{T_{\text{SM},c}}\right)^2 \approx H_c \left(\frac{T}{T_c}\right)^2. \quad (4.49)$$

The first step assumes that the SM dominates the Hubble parameter. In the last step we used the fact that the dark-to-SM temperature ratio is constant since both T and T_{SM} scale as the inverse of the scale factor. On the other hand, $T_f = T(\eta_f)$ is taken to be the moment when $F \ll 1$; we then set $-\ln F(\eta_f) = 10$, and thus

$$8\pi \frac{v_{\text{w}}^3(T_f)}{(\beta/H)^4(T_f)} \frac{\Gamma(T_i)}{H^4(T_f)} = 10 \Rightarrow 8\pi \frac{v_{\text{w}}^3(T_f)}{(\beta/H)^4(T_f)} \frac{\Gamma(T_f)}{H_c^4} \left(\frac{T_c}{T_f}\right)^8 \simeq 10. \quad (4.50)$$

A	λ_0	$\lambda_{0.95}$	$\lambda_{0.99}$	$\lambda_{0.995}$	$\lambda_{0.999}$
10^{-1}	0.129	0.183	0.303	0.380	0.647
10^{-2}	0.00600	0.00850	0.0140	0.0176	0.0300
10^{-3}	0.000279	0.000395	0.000652	0.000818	0.00139
10^{-4}	1.29×10^{-5}	1.83×10^{-5}	3.03×10^{-5}	3.80×10^{-5}	6.47×10^{-5}

Table 3. For each A , we determine the λ values where $T_0/T_c = 0.95, 0.99, 0.995, 0.999$ for $x_C = 0$. These are respectively denoted by $\lambda_{0.95}, \dots, \lambda_{0.999}$. Note that for each A , the ratios $\lambda_{0.95}/\lambda_0, \dots, \lambda_{0.999}/\lambda_0$ are respectively given by 1.416, 2.340, 2.936, and 5.004.

Then the time duration in which the dark sound speed exhibits a dip is

$$H_c(\eta_f - \eta_i) \approx \frac{1}{T_f/T_c} - \frac{1}{T_i/T_c}. \quad (4.51)$$

In the bottom panels of Fig. 3 we indicated the estimates for η_i and η_f as vertical dashed and dotted lines, respectively, and overlaid them on the $c_{s,D}^2$ curves. For these two BPs we can clearly see that our definitions of η_i and η_f provide us with a robust method to determine the width of the dip in $c_{s,D}^2$. As for the equation of state, note that w_D changes with conformal time via

$$w'_D = -3\mathcal{H}(1 + w_D)(c_{s,D}^2 - w_D), \quad (4.52)$$

which directly follows from the definition of sound speed and from the conservation of the dark fluid stress energy tensor. Eq. (4.52) can be rewritten as

$$\frac{d}{d(\ln a)} \ln(1 + w_D) = -3(c_{s,D}^2 - w_D). \quad (4.53)$$

Thus, the increase in w_D is expected to occur whenever $c_{s,D}^2 < w_D$. Note that the equation of state at the end of the FOPT $w_{\text{end}} \simeq \frac{p_{\text{TV}}}{\rho_{\text{TV}}}$ may, in general, not relax to the radiation equation of state $w_{\text{rad}} = 1/3$, as illustrated by the dashed curves in the bottom row of Fig. 3.

4.2.2 Parameter selection and scans over physical FOPT scenarios

We have shown in Section 2.1 that the physical conditions restrict the allowed regions in the $(L_c/T_c^4 - x_C)$ plane, for given A and λ . We observed that for a given A , a larger λ allows part of the physical region to reach values of T_0/T_c close to 1. Since the destabilization temperature T_0 determines the lower limit of the percolation temperature T_* , there are situations where T_* is guaranteed to be extremely close to T_c . We would like to avoid such scenarios, which correspond to small potential barriers. In Fig. 5 we plot, for a given value of A , the maximum range of L_c/T_c^4 and T_0/T_c values as functions of λ , which is achieved by setting $x_C = 0$. For sufficiently large λ , the maximum T_0/T_c approaches unity; correspondingly, the maximum value of L_c/T_c^4 is set by $g_\rho \pi^2/30 \simeq 1.48$. Furthermore, setting the maximum $T_0/T_c = 0.95, 0.99, 0.995, 0.999$ corresponds, respectively, to $\lambda/\lambda_0 \simeq 1.42, 2.34, 2.94, 5$, for $A = 10^{-1}, 10^{-2}, 10^{-3}, 10^{-4}$. The actual values of λ for each A are shown in Table 3, which provides us with a guide to select the benchmark points in Table 1.

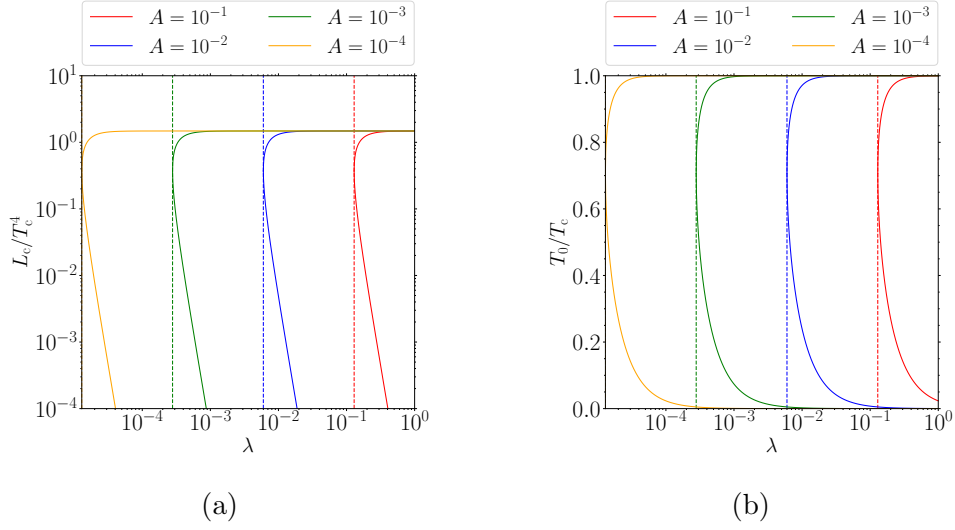


Figure 5. Panel (a) shows the allowed range of L_c/T_c^4 values versus λ , for each A value. Panel (b) shows the allowed range of T_0/T_c , for each A value. In both cases, $x_C = 0$; the vertical dashed lines indicate $\lambda_0(A)$.

Restricting our attention to physical FOPT scenarios, we would like to determine how the fundamental parameters that characterize the FOPT determine physically relevant quantities, such as the percolation temperature and the strength of the phase transition. This requires us to specify T_c and $r_{T,c}$, and then solve the system of ODEs that describe the background evolution. Firstly, in Fig. 6 we show scans of T_*/T_c . Here we take $A = 10^{-1}, 10^{-2}, 10^{-3}, 10^{-4}$. For each A , we choose $\lambda = 0.303, 1.4 \times 10^{-2}, 6.52 \times 10^{-4}, 3.03 \times 10^{-5}$, respectively, *i.e.* we fix $\lambda/\lambda_0 = 1.42$. We commit to $T_c = 10$ MeV and $r_{T,c} = 0.4$, unless we specify otherwise. For a fixed x_C , we find that the percolation temperature T_* tends to become closer to the critical temperature, along the direction of rescaled latent heat. This is expected behavior, knowing that T_0 also approaches T_c along this direction (see Fig. 1). We have checked that the general trend on T_* still holds for different T_c and $r_{T,c}$; also, the contours for fixed A and λ/λ_0 change only marginally. Thus, we find that imposing the condition that T_* is at most $0.95T_c$ restricts us from going close to the edge of the physical region towards the maximum rescaled latent heat.

In Fig. 7 we show scans of the FOPT strength, defined in Eq. (4.39). To understand the scans, we estimate α_* by noting that we are working in the regime where $\rho_{\text{SM}} \gg \rho_{\text{D}}$. This is required by the limit on

$$\Delta N_{\text{eff}} = \frac{4}{7} \left(\frac{11}{4} \right)^{4/3} g_{\rho} r_{T,c}^4 \simeq 0.25 \left(\frac{g_{\rho}}{4.5} \right) \left(\frac{r_{T,c}}{0.4} \right)^4 \leq 0.5, \quad (4.54)$$

from a combination of Planck and other data [44], which translates to $r_{T,c} < 0.474$. Then,

$$\rho_{\text{tot}} \approx \rho_{\text{SM}} \approx \frac{\pi^2}{30} \frac{g_{\rho, \text{SM}}}{r_{T,c}^4} T_*^4, \quad (4.55)$$

which gives

$$\alpha_* \approx \frac{1}{(T_*/T_c)^4} \left(1 - \frac{3}{4} \frac{T_*}{T_c} \right) \frac{L_c}{T_c^4} r_{T,c}^4. \quad (4.56)$$

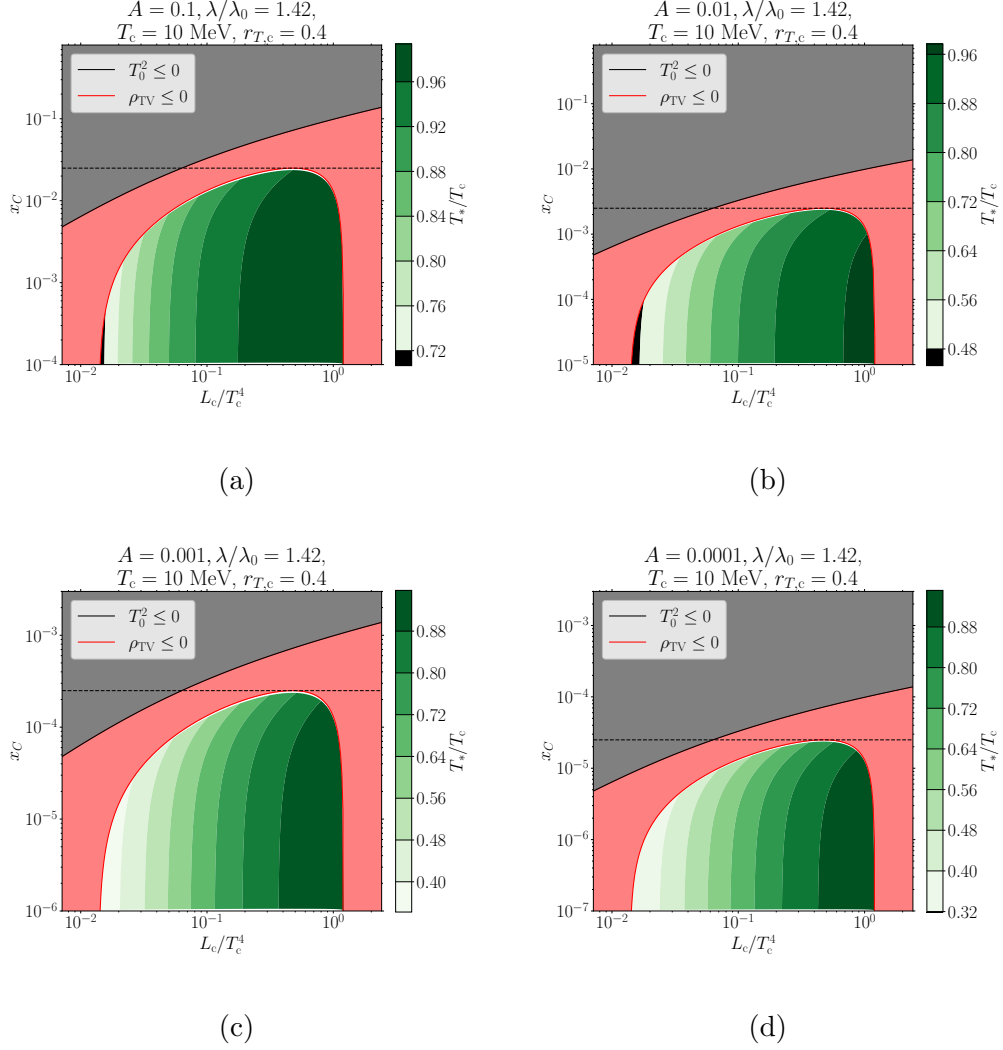


Figure 6. Contour plots of T_*/T_c for $A = 10^{-1}, 10^{-2}, 10^{-3}, 10^{-4}$, for fixed $\lambda/\lambda_0 = 1.42$, and $T_c = 10$ MeV, $r_{T,c} = 0.4$.

The trend in percolation temperature in Fig. 6, combined with the estimate for α_* in Eq. (4.56), are consistent with the scans of α_* in Fig. 7.

4.2.3 Perturbations during a FOPT

Once we know the background evolution during the FOPT, we can determine the evolution of each Fourier mode k/\mathcal{H}_c by solving Eqs. (4.3) and (4.4). In the following discussion, we assume that the single-fluid picture of the dark plasma holds for the perturbation modes of interest. The expressions for the average pressure, entropy density and energy density are provided in Eq. (4.44), and those for the equation of state and sound speed in Eq. (4.45).

Using the continuity and Euler equations in Eqs. (4.3) and (4.4) we explicitly write the

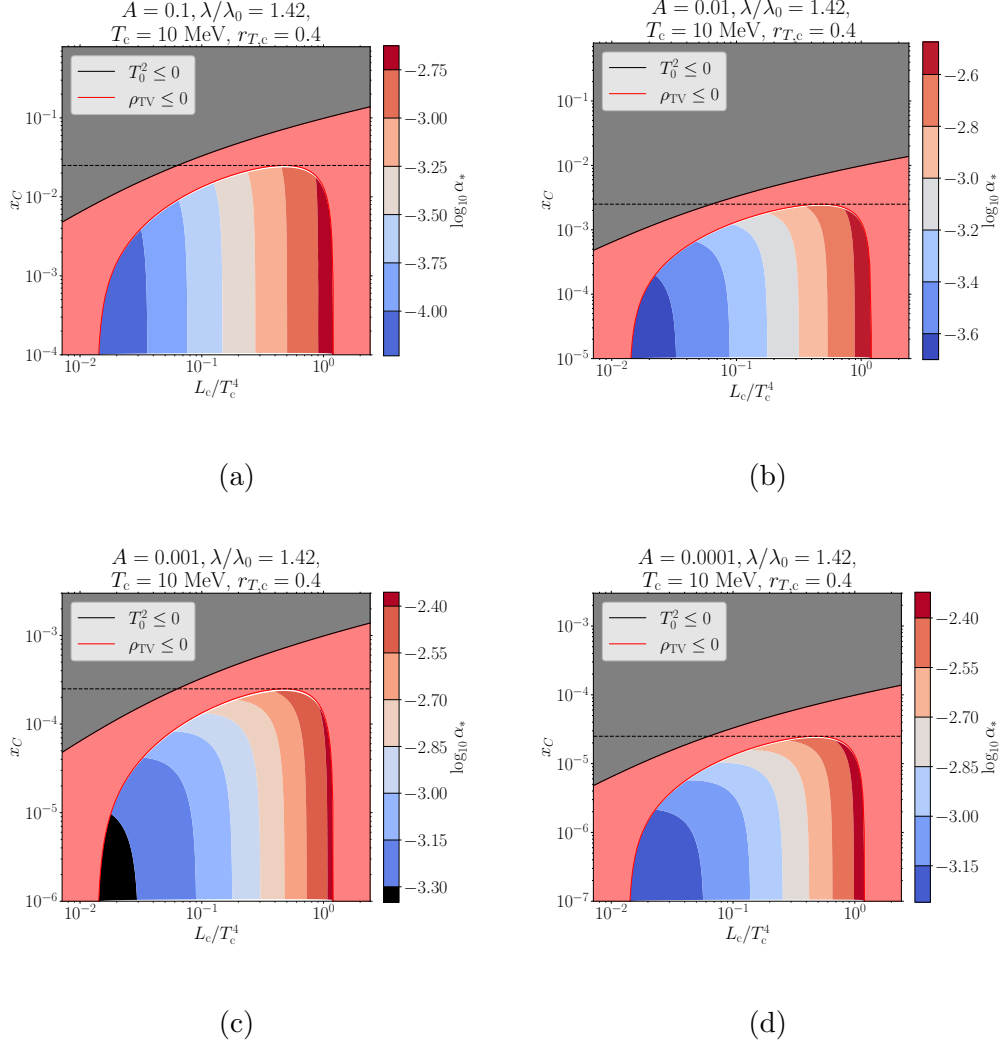


Figure 7. Contour plots of α_* for $A = 10^{-1}, 10^{-2}, 10^{-3}, 10^{-4}$, for fixed $\lambda/\lambda_0 = 1.42$, and $T_c = 10$ MeV, $r_{T,c} = 0.4$.

system of equations we need to solve. We have

$$\frac{\delta'_D}{\mathcal{H}} - \frac{k}{\mathcal{H}} \hat{\psi}_D + 3(1 + w_D) \Psi_k + 3(c_{s,D}^2 - w_D) \delta_D = 0, \quad (4.57)$$

$$\frac{\hat{\psi}'_D}{\mathcal{H}} + (1 - 3w_D) \hat{\psi}_D + c_{s,D}^2 \frac{k}{\mathcal{H}} \delta_D + (1 + w_D) \frac{k}{\mathcal{H}} \Psi_k = 0, \quad (4.58)$$

$$\frac{\delta'_{SM}}{\mathcal{H}} - \frac{k}{\mathcal{H}} \hat{\psi}_{SM} + 4\Psi_k = 0, \quad (4.59)$$

$$\frac{\hat{\psi}'_{SM}}{\mathcal{H}} + \frac{1}{3} \frac{k}{\mathcal{H}} \delta_{SM} + \frac{4}{3} \frac{k}{\mathcal{H}} \Psi_k = 0. \quad (4.60)$$

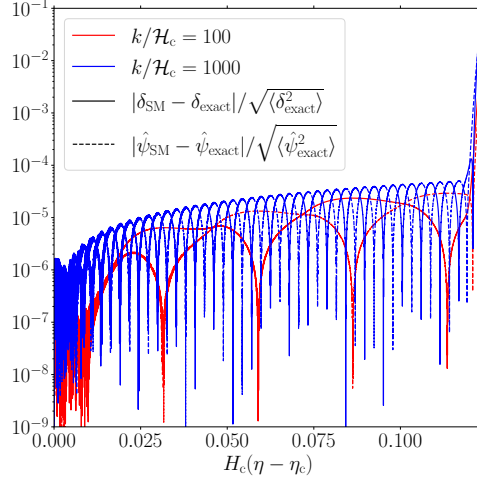


Figure 8. Comparison between exact δ and $\hat{\psi}$ evolution versus numerically calculated SM perturbations.

The gravitational potential Ψ_k is

$$\left[\left(\frac{k}{\mathcal{H}} \right)^2 + \frac{9}{2}(1+w) \right] \Psi_k + \frac{3}{2}(1+3c_s^2)\delta = 0, \quad (4.61)$$

where

$$\delta \equiv \frac{\rho_D \delta_D + \rho_{SM} \delta_{SM}}{\rho_D + \rho_{SM}}, \quad w \equiv \frac{\rho_D w_D + \rho_{SM} w_{SM}}{\rho_D + \rho_{SM}}, \quad c_s^2 \equiv \frac{\rho'_D c_{s,D}^2 + \rho'_{SM} c_{s,SM}^2}{\rho'_D + \rho'_{SM}}. \quad (4.62)$$

The gravitational potential Φ_k is

$$-k^2 \Phi_k = -\frac{3}{2} \mathcal{H}^2 \delta_k. \quad (4.63)$$

In the regime where $\rho_D \ll \rho_{SM}$, we have $|\rho'_D| \simeq |3\mathcal{H}\rho_D(1+w_D)| \ll |\rho'_{SM}|$. These imply that

$$\delta \simeq \delta_{SM}, \quad w \simeq w_{SM} \simeq c_s^2 \simeq c_{s,SM}^2 = 1/3, \quad (4.64)$$

so that

$$\Psi_k \approx -\frac{\delta_{SM,k}}{2 + \frac{1}{3} \left(\frac{k}{\mathcal{H}} \right)^2}. \quad (4.65)$$

The gravitational potential Φ appearing in the spatial part of the metric, which is relevant for the angular momentum calculation, is just

$$\Phi_k \simeq \frac{3}{2} \left(\frac{k}{\mathcal{H}} \right)^{-2} \delta_{SM,k}. \quad (4.66)$$

We first examine the behavior of the SM perturbations. In Fig. 8 we compare the numerical solutions for δ_{SM} and $\hat{\psi}_{SM}$ from solving the UHG perturbation equations during the FOPT,

and the result that one would obtain from the analytic expressions in Eq. (4.13), that are valid during the period when the dominant component of the Universe is a pure radiation fluid. Choosing BP-2, we plot the difference between the numerical result and the analytic result, normalized with respect to the RMS value of the analytic result within the period between the critical point and the percolation time, for the modes $k/\mathcal{H}_c = 100$ and $k/\mathcal{H}_c = 1000$. The difference is negligible, mainly because the equation of state and sound speed in the SM plasma are unaffected by the FOPT in the dark sector. To a good approximation, the analytic expressions for the perturbations in Eq. (4.13) can be extrapolated even during the period of FOPT for this benchmark case.

4.2.4 Superhorizon and subhorizon limits

Let us obtain the limiting behaviors of δ_D and $\hat{\psi}_D$ in the *superhorizon* and *subhorizon* limits. In the case $k/\mathcal{H} \ll 1$ and $\rho_{\text{SM}} \gg \rho_D$, the system of equations satisfied by the perturbations in the dark fluid reduce to

$$\delta'_D \approx k\hat{\psi}_D + \mathcal{H}(1 + 3c_{s,D}^2)\delta_{\text{SM}} - 3\mathcal{H}(c_{s,D}^2 - w_D)\delta_D, \quad (4.67)$$

$$\hat{\psi}'_D \approx -kc_{s,D}^2\hat{\psi}_D + \frac{k}{3}(1 + 3c_{s,D}^2)\delta_{\text{SM}} - \mathcal{H}(1 - 3w_D)\hat{\psi}_D. \quad (4.68)$$

Since $z \ll 1$, we may take $T_\delta(z) \approx 1$ and $dT_\delta/dz \approx 0$. We find that

$$\frac{d}{dz}\delta_D \approx \sqrt{3}\hat{\psi}_D - \frac{3(c_{s,D}^2 - w_D)}{z}\delta_D, \quad (4.69)$$

$$\frac{d}{dz}\hat{\psi}_D \approx -\frac{(1 - 3w_D)}{z}\hat{\psi}_D - \sqrt{3}c_{s,D}^2\delta_D, \quad (4.70)$$

where we have dropped terms containing positive powers of z and higher. We can compare these with [21], which found that the evolution of the perturbations in the superhorizon limit is independent of the sound speed. This applies in our case if the dominant fluid component, which mainly dictates the Hubble expansion, is the dark fluid. One can show that the continuity equation can be rewritten as

$$\frac{d}{dz} \ln \left(\frac{\delta_D}{1 + w_D} \right) \approx \sqrt{3} \frac{\hat{\psi}_D}{\delta_D}. \quad (4.71)$$

Similarly, it follows from Eqs. (4.67) and (4.68) that

$$\frac{d}{dz} \left(\frac{\hat{\psi}_D}{\delta_D} \right) \approx \frac{(3c_{s,D}^2 - 1)}{z} \left(\frac{\hat{\psi}_D}{\delta_D} \right) - \sqrt{3}c_{s,D}^2 - \sqrt{3} \left(\frac{\hat{\psi}_D}{\delta_D} \right)^2. \quad (4.72)$$

From the initial conditions for $\hat{\psi}_D$ and δ_D , we have $(\hat{\psi}_D/\delta_D)_c \propto z_c$. To leading order, we have

$$\frac{\hat{\psi}_D}{\delta_D} \approx C_0 z, \quad C_0 \equiv \frac{\sqrt{3}c_{s,D}^2}{3c_{s,D}^2 - 2}. \quad (4.73)$$

Then we have

$$\delta_D \approx \delta_{D,c} \frac{1 + w_D}{1 + w_{D,c}} \exp \left[\frac{\sqrt{3}C_0}{2}(z^2 - z_c^2) \right] \approx \delta_{D,c} \frac{1 + w_D}{1 + w_{D,c}} \left[1 + \frac{\sqrt{3}C_0}{4}(z^2 - z_c^2) \right]. \quad (4.74)$$

On the other hand, the approximate solutions in the *subhorizon* regime can be worked out by starting from the subhorizon limit of the evolution equations for the perturbations

$$\delta'_D \approx k\hat{\psi}_D - 3\mathcal{H}(c_{s,D}^2 - w_D)\delta_D, \quad \hat{\psi}'_D \approx -kc_{s,D}^2\delta_D - \mathcal{H}(1 - 3w_D)\hat{\psi}_D. \quad (4.75)$$

Note that the Ψ_k term which involves the weighted sum of all density perturbations, can be dropped for $k/\mathcal{H} \gg 1$. We can use Eq. (4.75), together with (4.52), to write down a single second order ODE for δ_D , given by

$$\delta''_D + (3c_{s,D}^2 - 6w_D + 1)\mathcal{H}\delta'_D + [k^2c_{s,D}^2 + 9\mathcal{H}^2(c_{s,D}^2 - w_D) + 3\mathcal{H}(c_{s,D}^2)']\delta_D \approx 0. \quad (4.76)$$

A similar expression was found in [21], apart from the extra terms appearing in the δ_D term. In the WKB regime, we assume that the oscillation period of the Fourier mode under consideration is much shorter than the scale of the time variation of the sound speed and of $c_{s,D}^2 - w_D$, *i.e.*

$$k^2c_{s,D}^2 \gg \mathcal{H} \frac{1}{c_{s,D}^2} (c_{s,D}^2)', \quad k^2c_{s,D}^2 \gg \mathcal{H}^2 (c_{s,D}^2 - w_D). \quad (4.77)$$

Following [21], we introduce

$$\delta_D = \frac{H_c^2(1 + w_D)^{1/2}}{a^2\rho_D^{1/2}}u_D, \quad (4.78)$$

to eliminate the drag term. The ODE satisfied by u_D is then

$$u''_D + k^2c_{s,D}^2(\eta)u_D \approx 0, \quad (4.79)$$

where we essentially took the zeroth order coefficient to be dominated by the time dependent frequency $\omega(\eta) \equiv kc_{s,D}(\eta)$. The WKB solution then becomes

$$u_D(\eta) \approx [c_{s,D}^2(\eta)]^{-1/4} [a_k \sin \phi_k(\eta) + b_k \cos \phi_k(\eta)], \quad \phi_k(\eta) \equiv k \int_{\eta_c}^{\eta} d\eta' c_{s,D}(\eta'). \quad (4.80)$$

Armed with the WKB approximation to u_D , we can use Eq. (4.78) to obtain δ_D . For a given Fourier mode, the coefficients a_k and b_k are chosen to match the initial conditions, which are expressed in terms of δ_D and δ'_D , where

$$\delta_D(\eta_c) = \delta_{SM}(z_c), \quad \delta'_D(\eta_c) = \hat{\psi}_{SM}(z_c) \sqrt{3}\mathcal{H}_c z_c. \quad (4.81)$$

Meanwhile, we have

$$\hat{\psi}_D \approx \frac{\delta'_D}{k}, \quad (4.82)$$

which we can use to obtain $\hat{\psi}_D$.

4.2.5 Numerical scheme

To determine the transfer functions during the FOPT, we first numerically solve the background evolution equations, Eqs. (4.28)-(4.33), and then work out the perturbation equations, given in Eqs. (4.57)-(4.60) for a given mode k/\mathcal{H}_c and for a fluid component (SM or dark sector), up to the percolation time. Since the perturbations are crucial for the calculation of the angular momentum of FV remnants, it is necessary to perform checks on our numerical scheme. We can compare our numerical transfer functions

$$U_{Q_I} \equiv \frac{Q_I}{\mathcal{R}_k}, \quad Q_I = \delta_D, \hat{\psi}_D, \Phi, \nabla^2 \gamma,$$

with the WKB approximation and the SM perturbations, for subhorizon modes.

In Fig. 9 we show plots of U_δ (top row) and $U_{\hat{\psi}}$ (bottom row) as functions of the rescaled elapsed conformal time, for BP-2 and BP-7, as in Fig. 3, where we fix $k/\mathcal{H}_c = 1000$. In all panels, the solid curves correspond to the dark sector perturbation, the dashed curves correspond to the corresponding SM perturbation, and the dotted curves correspond to the WKB approximation. In all cases, we observe excellent agreement between the WKB approximation and the numerical solution. There is a deviation between the two results close to the percolation time, which is at the right-most edge of each panel. This discrepancy between the numerical solution and the WKB approximation can be understood by noting that $c_{s,D}^2$ is no longer a slowly varying function close to the percolation time.

Ultimately, in calculating the angular momentum of FV remnants, we need the transfer functions at the percolation time. In Fig. 10, we show the absolute values of the transfer functions, evaluated at the percolation time, for modes within $0.1 < k/\mathcal{H}_c < k_{\text{cut}}$, where $k_{\text{cut}} = 5/(H_* R_*)$, H_* is the Hubble parameter at percolation, and R_* is the physical radius of a FV bubble at percolation. We take the physical radius R_* of the FV bubble at percolation to be

$$n_{\text{FV}}(t_*) \frac{4\pi}{3} R_*^3 = F_*, \quad (4.83)$$

where $n_{\text{FV}}(t_*)$ is the number density of FV bubbles at the percolation time. Equivalently, this critical radius R_* is determined from the condition that no TV bubble nucleates inside, so that

$$\Gamma(t_*) \frac{R_*}{v_{w,*}} \frac{4\pi R_*^3}{3} = 1. \quad (4.84)$$

It is straightforward to show that

$$R_* = \left(\frac{3}{4\pi} \right)^{1/4} \left(\frac{v_{w,*}}{\Gamma_*} \right)^{1/4}. \quad (4.85)$$

In panels (a) and (b) of Fig. 10, we can see that the superhorizon modes follow the expected scaling behaviors $\delta_D \propto (k/\mathcal{H})^2$ and $\hat{\psi}_D \propto (k/\mathcal{H})^3$. In the subhorizon regime $k/\mathcal{H}_c \gtrsim 1$, the rapid oscillations of U_δ and $U_{\hat{\psi}}$ are manifestations of the WKB behavior of the solutions in the deep subhorizon regime. For perturbative modes $k/\mathcal{H}_c > 10^2$, we observe an enhancement in the transfer functions for the density perturbations. We can attribute this to the period when $c_{s,D}^2$ exhibits a dip around the percolation time, as seen in the bottom row of Fig. 3. This behavior is similar to the main results of [21], where the vanishing sound speed

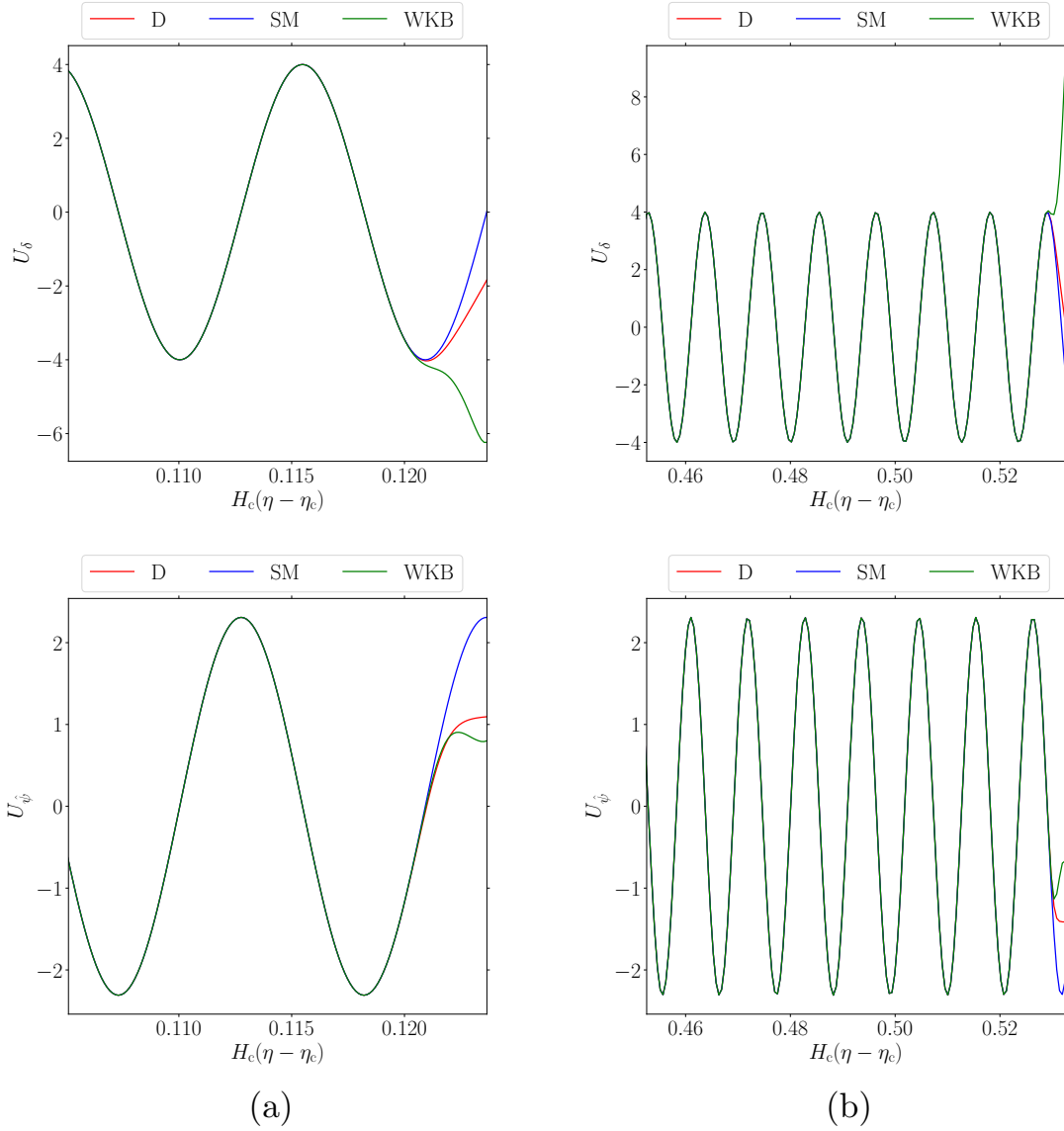


Figure 9. The density (top row) and velocity (bottom row) perturbations for benchmarks BP-2 (column a) and BP-7 (column b) for $k/\mathcal{H}_c = 10^3$.

of the plasma leads to an enhancement in the density perturbations. In both benchmarks BP-2 and BP-7, the width of the dip is $\mathcal{H}_c(\eta_f - \eta_i) \simeq 4.2 \times 10^{-3}$, indicating that those modes with wavenumbers of around at least $k/\mathcal{H}_c \simeq \frac{1}{\mathcal{H}_c(\eta_f - \eta_i)} \simeq 250$, will have enough resolution to resolve the dip feature in the temporal evolution of the sound speed.

Since the WKB approximation breaks down at the percolation time, we can understand the behavior of the transfer functions in the subhorizon regime by accounting for the sharp decrease in the sound speed at around the percolation time. We solve the ODE,

$$\delta_D'' + k^2 c_{s,D}^2 \delta_D \approx 0, \quad (4.86)$$

where we have implicitly assumed that the drag term can be dropped. This is justified

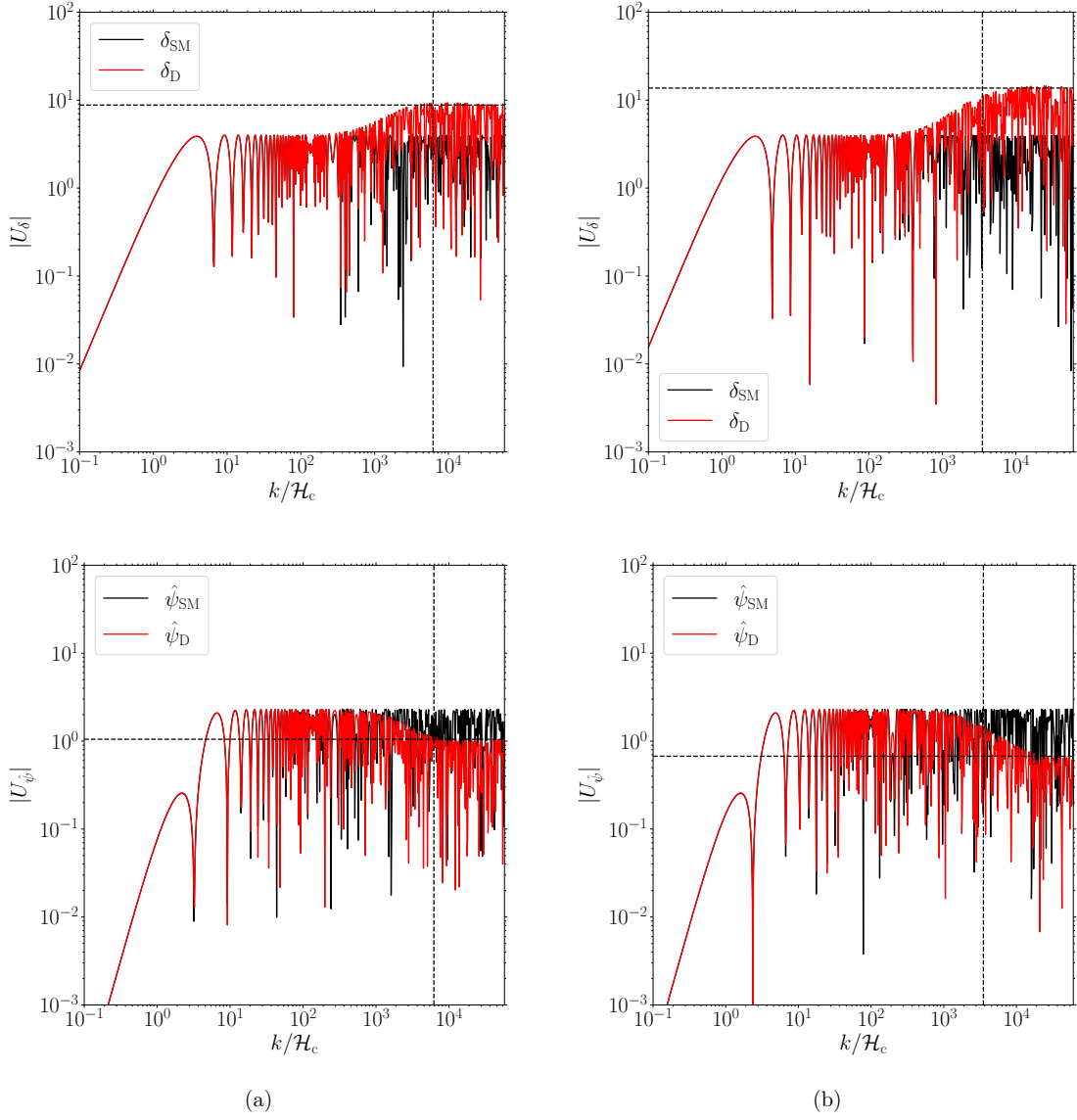


Figure 10. The absolute sizes of U_δ, U_ψ at the percolation time, for a range of modes $10^{-3} < k/\mathcal{H}_c < (k/\mathcal{H}_c)_{\text{cut}}$, and taking FOPT benchmarks BP-2 (column a) and BP-7 (column b) as in Fig. 3.

provided that

$$(3c_{s,D}^2 - 6w_D + 1) \left(\frac{k}{\mathcal{H}} \right) c_{s,D} \ll \left(\frac{k}{\mathcal{H}} \right)^2 c_{s,D}^2 + 9\mathcal{H}^2 (c_{s,D}^2 - w_D) + 3\mathcal{H} (c_{s,D}^2)'. \quad (4.87)$$

Then we approximate $c_{s,D}^2$ by a piecewise linear function where

$$c_{s,D}^2 \approx \begin{cases} \frac{1}{3}, & 0 \leq \tilde{\eta} \leq \tilde{\eta}_i \\ \frac{1}{3} + \left(\frac{c_{s,D*}^2 - 1/3}{\tilde{\eta}_* - \tilde{\eta}_i} \right) (\tilde{\eta} - \tilde{\eta}_i), & \tilde{\eta}_i < \tilde{\eta} \leq \tilde{\eta}_*. \end{cases} \quad (4.88)$$

In the interval $0 \leq \tilde{\eta} \leq \tilde{\eta}_i$ the solution is simply a superposition of sines and cosines given by

$$\delta = \delta_c \cos\left(\frac{1}{\sqrt{3}} \frac{k}{\mathcal{H}_c} \tilde{\eta}\right) + \sqrt{3} \hat{\psi}_c \sin\left(\frac{1}{\sqrt{3}} \frac{k}{\mathcal{H}_c} \tilde{\eta}\right), \quad (4.89)$$

where δ_c and $\hat{\psi}_c$ are the perturbations evaluated at the critical point, assuming the analytic expression for perturbations evolving in a pure radiation background. On the other hand, in the interval $\tilde{\eta}_i < \tilde{\eta} \leq \tilde{\eta}_*$, the ODE admits a general solution in terms of Airy functions

$$\delta = c_1 Ai(u) + c_2 Bi(u), \quad u \equiv \frac{-d_1 - d_2 \tilde{\eta}}{(-d_2)^{2/3}}, \quad (4.90)$$

where

$$d_1 = \frac{1}{3} \left(\frac{k}{\mathcal{H}_c}\right)^2 \left[1 - 3\tilde{\eta}_i \left(\frac{c_{s,D*}^2 - 1/3}{\tilde{\eta}_* - \tilde{\eta}_i}\right)\right], \quad d_2 = \left(\frac{k}{\mathcal{H}_c}\right)^2 \left(\frac{c_{s,D*}^2 - 1/3}{\tilde{\eta}_* - \tilde{\eta}_i}\right). \quad (4.91)$$

The coefficients c_1 and c_2 are obtained by matching the solutions at $\tilde{\eta} = \tilde{\eta}_i$. The density and velocity perturbations at the percolation time will then be

$$\delta_* = c_1 Ai(u_*) + c_2 Bi(u_*), \quad \hat{\psi}_* = \frac{1}{k/\mathcal{H}_c} (-d_2)^{1/3} [c_1 Ai'(u_*) + c_2 Bi'(u_*)], \quad (4.92)$$

where $u_* \equiv (-d_1 - d_2 \tilde{\eta}_*)(-d_2)^{-2/3}$.

We can further understand the approximate transfer functions by performing an asymptotic expansion in powers of k/\mathcal{H}_c . We find

$$\begin{aligned} \delta_* \approx & -\frac{4}{(3c_{s,D*}^2)^{1/4}} \cos \phi_- \\ & + \frac{1}{k/\mathcal{H}_c} \left[\left(\frac{5\sqrt{3}(c_s^2)' - 288(c_{s,D*}^2)^{3/2} + 9(c_s^2)'(c_{s,D*}^2)^{3/2}}{12 \cdot 3^{3/4} (c_{s,D*}^2)^{7/4}} \right) \sin \phi_- \right. \\ & \left. - \frac{3}{2} \left(\frac{3}{c_{s,D*}^2} \right)^{1/4} (c_s^2)' \sin \phi_+ \right], \end{aligned} \quad (4.93)$$

and

$$\begin{aligned} \hat{\psi}_* \approx & \frac{4}{\sqrt{3}} (3c_{s,D*}^2)^{1/4} \mathcal{R}_k \sin \phi_- \\ & + \frac{\mathcal{R}_k}{k/\mathcal{H}_c} \left[\left(\frac{7\sqrt{3}(c_s^2)' + 288(c_{s,D*}^2)^{3/2} - 9(c_s^2)'(c_{s,D*}^2)^{3/2}}{12 \cdot 3^{3/4} (c_{s,D*}^2)^{5/4}} \right) \cos \phi_- \right. \\ & \left. - \frac{3}{2} (3c_{s,D*}^2)^{1/4} \cos \phi_+ \right]. \end{aligned} \quad (4.94)$$

Here

$$\phi_{\pm} \equiv \frac{1 + \tilde{\eta}_i}{\sqrt{3}} \frac{k}{\mathcal{H}_c} \pm \frac{2}{27(c_s^2)'} \left(\sqrt{3} - 9(c_{s,D*}^2)^{3/2} \right) \frac{k}{\mathcal{H}_c}, \quad (4.95)$$

$$(c_s^2)' \equiv -\frac{1/3 - c_{s,D*}^2}{\tilde{\eta}_* - \tilde{\eta}_i}. \quad (4.96)$$

By comparison, the asymptotic values for $k/\mathcal{H}_c \gg 1$ in the *pure radiation background case* are

$$\delta_* \rightarrow -4\mathcal{R}_k \cos\left(\frac{1}{\sqrt{3}}\frac{k}{\mathcal{H}_c}(1 + \tilde{\eta}_*)\right), \quad \hat{\psi}_* \rightarrow \frac{4}{\sqrt{3}}\mathcal{R}_k \sin\left(\frac{1}{\sqrt{3}}\frac{k}{\mathcal{H}_c}(1 + \tilde{\eta}_*)\right). \quad (4.97)$$

We recover the result for radiation when $c_{s,D*}^2 \rightarrow 1/3$. For $k/\mathcal{H}_c \gg 1$, we find that the asymptotic value of $|\delta_*|$ is *enhanced* relative to the pure radiation background by a factor of $(3c_{s,D*}^2)^{-1/4}$. Similarly, $|\hat{\psi}_*|$ will be *suppressed* by the same factor. These estimates for the enhancement/suppression in the density/velocity transfer functions, for sufficiently large k/\mathcal{H}_c , are shown as horizontal dashed lines in Fig. 10. We clearly see that the estimates match the results of numerical calculation.

Modes with sufficiently long wavelengths are marginally affected by the sudden drop in $c_{s,D}^2$, and thus the amplitude of the density (velocity) transfer function for such modes approaches 4 ($4/\sqrt{3}$). The transition to the asymptotic values of the transfer function for $k/\mathcal{H}_c \gg 1$ must be continuous, as shown by the transfer functions in Fig. 11. We generated those transfer functions, under the assumption that we approximate the sound speed squared as a piecewise linear function in rescaled conformal time. The range of k -modes that connect the amplitudes of the transfer functions for small k and large k , can be obtained as follows. From physical grounds, modes that satisfy

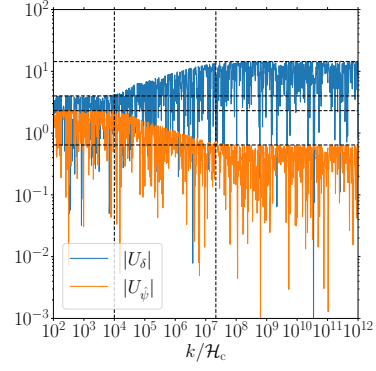
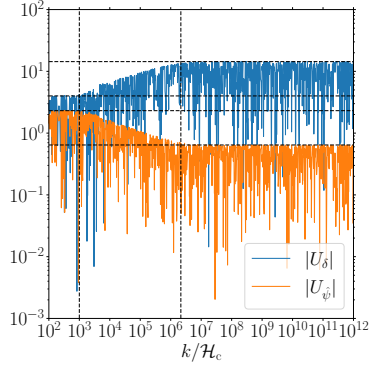
$$\frac{k}{\mathcal{H}_c} \gtrsim \frac{1}{\tilde{\eta}_* - \tilde{\eta}_i} \quad (4.98)$$

will have sufficient temporal resolution to be affected by the decrease in $c_{s,D}^2$ around the percolation time. The corresponding density modes will undergo enhancement to $4/(3c_{s,D*}^2)^{1/4}$, up to a certain k -mode where the next-to-leading order term in Eq. (4.93) is subdominant; an analogous statement can also be said for the velocity modes. Meanwhile, an upper limit in k/\mathcal{H}_c , beyond which the density and velocity transfer functions are guaranteed to be quenched to their asymptotic values, is

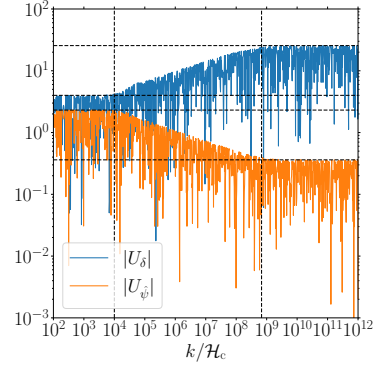
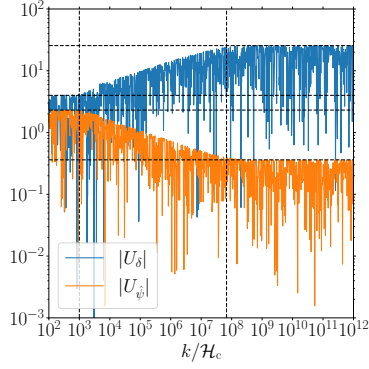
$$\frac{k}{\mathcal{H}_c} < \frac{1}{(3c_{s,D*}^2)^{3/2}(\tilde{\eta}_* - \tilde{\eta}_i)}. \quad (4.99)$$

In Fig. 11, vertical dashed lines mark the range of modes identified by Eqs. (4.98) and (4.99).

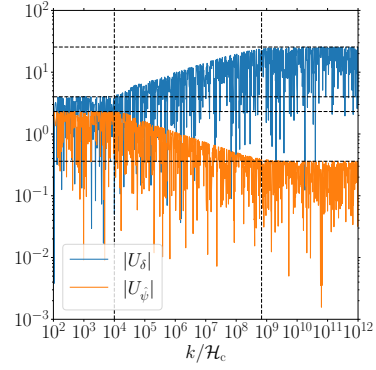
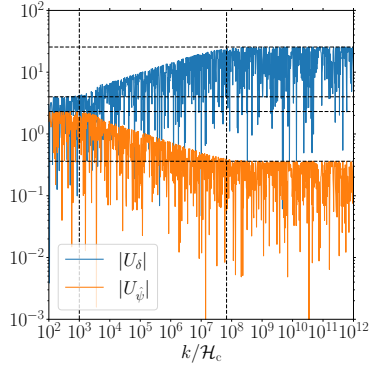
The approximate treatment of assuming a linear drop in $c_{s,D}^2$ allows us to identify the factors that affect the transfer functions, namely: the period $\tilde{\eta}_* - \tilde{\eta}_i$ when the drop in $c_{s,D}^2$ occurs; and the sound speed squared $c_{s,D*}^2$ at the percolation time. We demonstrate the effect of these quantities on the transfer functions in Fig. 11. In the top row we changed $\tilde{\eta}_* - \tilde{\eta}_i$, effectively changing the width of the dip in $c_{s,D}^2$ (across columns). As expected, reducing the width simply moves the locations of the vertical lines that mark those modes that suffer enhancement in the density. For the middle row, we changed $c_{s,D*}^2$ (from top to middle row). Decreasing $c_{s,D*}^2$ increases/decreases the quenched values of the density/velocity transfer functions in the large k/\mathcal{H}_c limit. The bottom row features transfer functions for a longer FOPT duration. In keeping the width and $c_{s,D*}^2$ the same as in the middle row, we do not see any noticeable change in behavior in the transfer functions. Finally, in Fig. 10, the horizontal dashed lines demonstrate that our estimates for the amount of enhancement/suppression in the density/velocity transfer functions match the results of numerical calculation.



$$\tilde{\eta}_i = 0.1 - 10^{-3}, \tilde{\eta}_* = 0.1, c_{s,D*}^2 = 2 \times 10^{-3} \quad \tilde{\eta}_i = 0.1 - 10^{-4}, \tilde{\eta}_* = 0.1, c_{s,D*}^2 = 2 \times 10^{-3}$$



$$\tilde{\eta}_i = 0.1 - 10^{-3}, \tilde{\eta}_* = 0.1, c_{s,D*}^2 = 2 \times 10^{-4} \quad \tilde{\eta}_i = 0.1 - 10^{-4}, \tilde{\eta}_* = 0.1, c_{s,D*}^2 = 2 \times 10^{-4}$$



$$\tilde{\eta}_i = 1 - 10^{-3}, \tilde{\eta}_* = 1, c_{s,D*}^2 = 2 \times 10^{-4} \quad \tilde{\eta}_i = 1 - 10^{-4}, \tilde{\eta}_* = 1, c_{s,D*}^2 = 2 \times 10^{-4}$$

Figure 11. The density and velocity transfer functions, approximating $c_{s,D}^2$ via Eq. (4.88), when the width of $c_{s,D}^2$ (i.e. changing $\tilde{\eta}_i$) or the sound speed squared at percolation (i.e. changing $c_{s,D*}^2$) is changed. In the last row, we also changed the duration of the FOPT, by a factor of 10, while still keeping the width $\tilde{\eta}_* - \tilde{\eta}_i$.

5 Results and discussion

5.1 Numerical values of physical quantities

To calculate the RMS angular momentum and spin of a sphere of dark plasma at the percolation time, we use Eq. (3.42), which requires us to know the enclosed mass and physical radius, as well as the coefficient $\mathcal{C}(\tilde{x}_0, x_0)$. For an arbitrary conformal time η and \tilde{x}_0 , the RMS values of the angular momentum and spin at any given time can be calculated from

$$J_{\text{CM,rms}}(\eta) = M(\eta)R(\eta)v_{\text{eff}}, \quad s_{\text{rms}} = \frac{R(\eta)}{G_N M(\eta)}v_{\text{eff}}, \quad (5.1)$$

$$M(\eta) = \frac{4\pi}{3}R^3(\eta)\rho_D(\eta), \quad v_{\text{eff}} = \frac{3}{4}A_s\tilde{x}_0(\eta)\mathcal{C}^{1/2}(\tilde{x}_0, x_0). \quad (5.2)$$

From Eq. (5.2) we see that the spin is a product of $R/(G_N M)$, the inverse of the surface potential, and v_{eff} , the effective *equatorial velocity* of the FV remnant. The inverse of the surface potential can be calculated by knowing only the background evolution, whereas v_{eff} requires the \mathcal{C} function. At percolation, we simply evaluate $\mathcal{C}(\tilde{x}_0, x_0)$ at $\tilde{x}_0 = \sqrt{3}\mathcal{H}_*x_{0,*} = \sqrt{3}H_*R_*$, which we will then denote by \mathcal{C}_* .

The coefficient \mathcal{C}_* , expressed as an integral in Eq. (3.43) and evaluated at the percolation time, contains explicit dependence on the primordial power spectrum of curvature perturbations, and the transfer functions for all k modes. However, from a practical standpoint, only a finite number of modes can be calculated numerically. We have chosen to solve the perturbation equations up to the percolation time, for $N = 1000$ modes between $10^{-3} < k/\mathcal{H}_c < 5/(H_*R_*)$ that are uniformly spaced in logarithm, and construct a table of values for $\delta_{D,*}$, $\hat{\psi}_{D,*}$, Φ_* , and $-k^2\gamma_*$ versus k/\mathcal{H}_* . Then, for an arbitrary k/\mathcal{H}_* , we can evaluate these perturbations from the table by interpolation. We then perform the \mathcal{C}_* integration using a general purpose Monte Carlo integrator, and by setting the cutoff at

$$k_{\text{cut}} = \frac{\pi}{R_*}, \quad (5.3)$$

which corresponds to a mode whose wavelength matches the FV bubble diameter. We do not consider modes that are shorter than k_{cut} , since they can resolve between false and true vacuum regions, such that the dark plasma can no longer be considered as a single entity.

In Fig. 12 we show the dependence of \mathcal{C}_* and $v_{\text{eff},*}$ on the bubble size relative to Hubble in red and blue, respectively. The two panels feature BP-2 and BP-7. The dotted lines, corresponding to the SM approximation, use the exact transfer functions in Eqs. (4.14), to calculate \mathcal{C}_* and $v_{\text{eff},*}$, with integration up to $k = \pi/R_*$. The vertical line marks the size of the FV bubble $R_{\text{FV},*}$ relative to Hubble, associated with the prescription in Eq. (4.83). As we can see in Fig. 12, the difference between the dark sector $v_{\text{eff},*}$ and the SM approximation is at most an order 1 factor. The drop in both \mathcal{C}_* and $v_{\text{eff},*}$ for $\tilde{x}_{0,*} < \sqrt{3}H_*R_{\text{FV},*}$ is associated with the fact that k_{cut} is above the largest k mode available in the interpolation table; whenever we encounter this case, we extrapolate the transfer functions to zero. For the benchmark points in Fig. 12, the relative size of the FV bubble, \mathcal{C}_* , $v_{\text{eff},*}$, and $s_{\text{rms},*}$, can be found in Table 1. We find that the FV bubbles are much smaller than the Hubble horizon and the effective equatorial velocity is much smaller than the speed of light.

5.2 Estimates and scans over the physical region

From Eq. (5.1), the RMS spin of FV bubbles can be expressed in terms of the inverse of the surface potential $R_*/(G_N M_*)$ and the equatorial velocity. The former can be directly

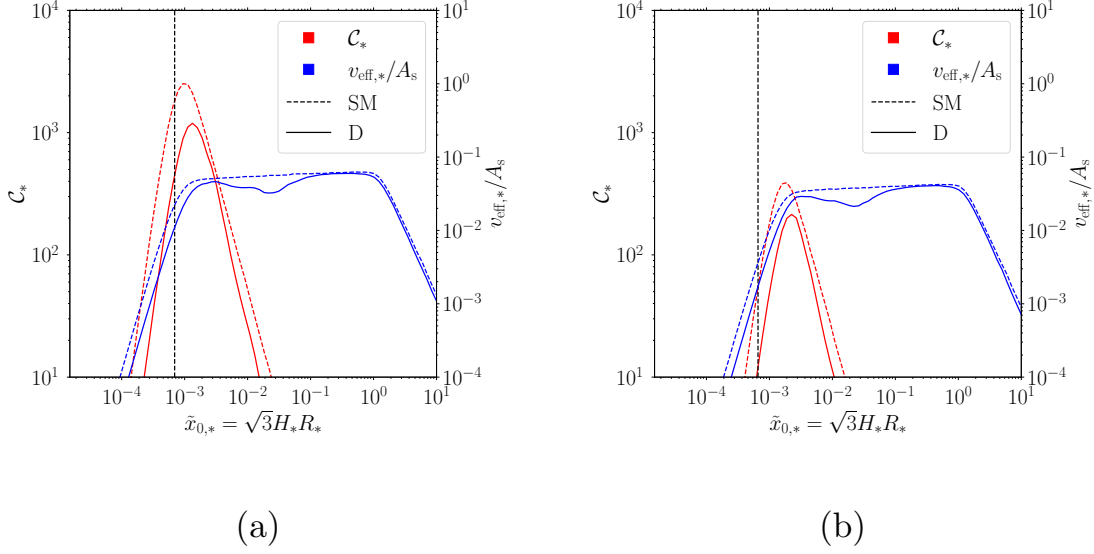


Figure 12. \mathcal{C}_* and $v_{\text{eff},*}$ versus $\tilde{x}_{0,*}$ for the FOPT benchmark cases BP-2 (panel a) and BP-7 (panel b) in Fig. 3. The vertical line marks the size of the FV bubble $R_{\text{FV},*}$ relative to Hubble constant at percolation.

estimated from the background evolution as follows. In our prescription, R_* is given by Eq. (4.83), and the FV fraction is given by Eq. (4.41). We can trade Γ_* with β_* to find

$$R_* \approx 6^{1/4} \frac{v_{\text{w},*}}{\beta_*}. \quad (5.4)$$

The mass of the FV bubble requires R_* and $\rho_{D,*}$, with the latter given by

$$\rho_{D,*} = \frac{\pi^2}{30} g_\rho T_*^4 - (1 - F_*) L_c. \quad (5.5)$$

We can relate $\rho_{D,*}$ with the Hubble scale through the total energy density:

$$\rho_{\text{tot},*} = \frac{\pi^2}{30} g_{\rho,\text{SM}}(T_*) \frac{T_*^4}{r_{T,c}^4} + \frac{\pi^2}{30} g_\rho T_*^4 - (1 - F_*) L_c = \frac{3H_*^2}{8\pi G_N}. \quad (5.6)$$

We now formulate the following estimate for the RMS spin, which constitutes one of our main results:

$$s_{\text{rms},*} \approx \left(\frac{2}{3} \right)^{1/2} \left(\frac{\beta_*/H_*}{v_{\text{w},*}} \right)^2 \frac{g_{\rho,\text{SM}}(T_*)}{g_*} r_{T,c}^{-4} \left[1 - (1 - F_*) \frac{30}{\pi^2 g_\rho} \frac{L_c}{T_c^4} \left(\frac{T_c}{T_*} \right)^4 \right]^{-1} v_{\text{eff},*}. \quad (5.7)$$

Note that the explicit dependence of $s_{\text{rms},*}$ on v_{w} means that the spin depends on the exponent k in in Eq. (4.23). For BP-2 and BP-7, we have checked that for k values from 2 to 8, the spin gradually decreases by a factor roughly equal to $[1 - (T_*/T_c)^8]^2 / [1 - (T_*/T_c)^2]^2$. Note that β_*/H_* , $v_{\text{eff},*}$, and T_* are marginally sensitive to k . One can show that the term in square brackets is significant when L_c/T_c^4 hits the maximum possible value allowed by the

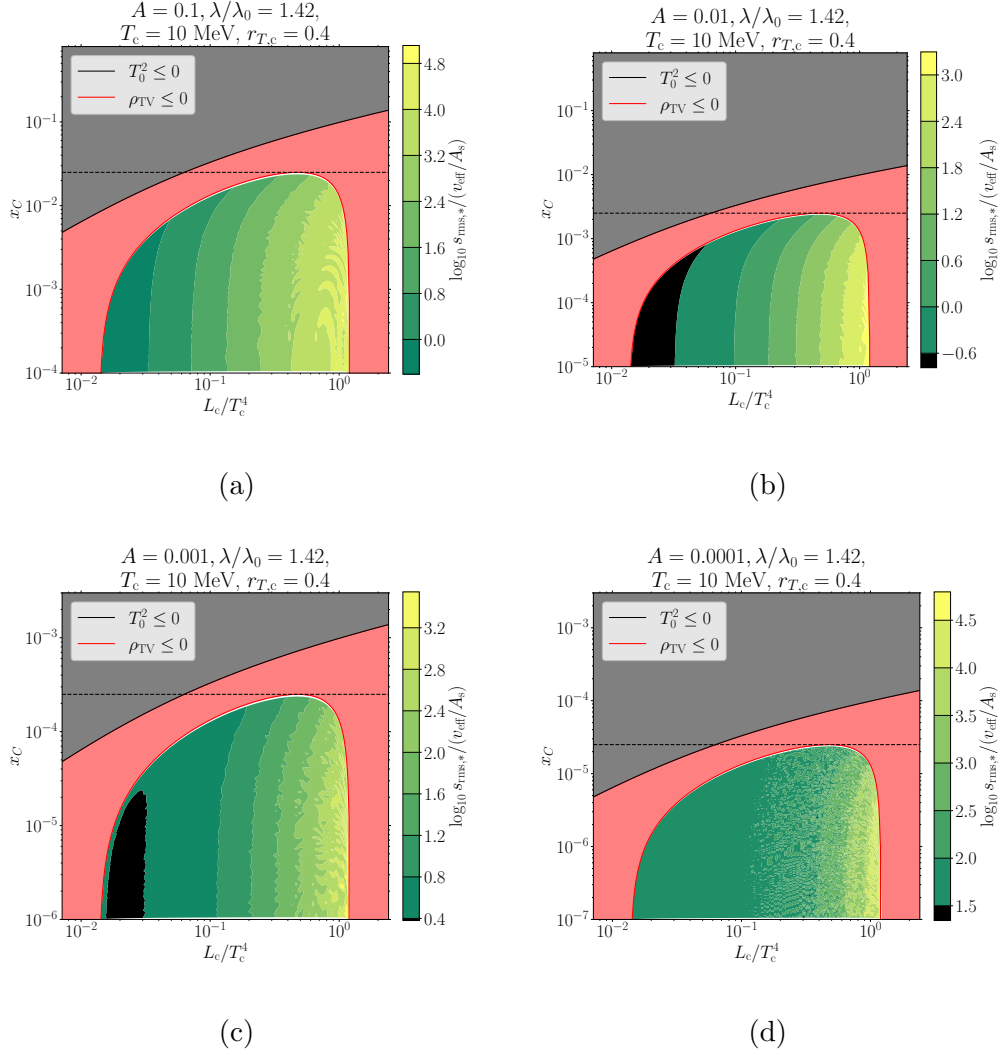


Figure 13. Contour plots of $s_{\text{rms},*}/(v_{\text{eff},*}/A_s)$ for $A = 10^{-1}, 10^{-2}, 10^{-3}, 10^{-4}$, for fixed $\lambda/\lambda_0 = 1.42$, and $T_c = 10 \text{ MeV}$, $r_{T,c} = 0.4$.

physical conditions; otherwise, for $L_c/T_c^4 \ll g_\rho \pi^2/30$, the term in square brackets is simply F_* . On the other hand, we typically find that $v_{\text{eff},*}/A_s$ is in the range $\sim 10^{-3}$ to $\sim 10^{-2}$. We have found that the value of $v_{\text{eff},*}/A_s$ is sensitive to the spectral index n_s of the primordial curvature power spectrum. In the case where $n_s = 1$, $v_{\text{eff},*}/A_s$, and thus the spin value, is enhanced by roughly an order of magnitude.

We then combine this result with the scans of $s_{\text{rms},*}/(v_{\text{eff},*}/A_s)$ in the physical region shown in Fig. 13. Although it is possible to obtain values of $s_{\text{rms},*}$ that are less than unity, there are cases where the RMS spin can exceed it. Note that a large spin value does not pose a problem because the FV bubble is not a black hole. For comparison, we list some typical dimensionless spin values for a few astrophysical objects in Table 4.

We can see from Fig. 13 that a wide range of $s_{\text{rms},*}/(v_{\text{eff},*}/A_s)$ values can be obtained, even for fixed A and λ , and fixed T_c and $r_{T,c}$. Equation (5.7) explains this behavior because the percolation temperature and β_*/H_* vary widely within the physical region. Furthermore,

	Sun	Earth	Neutron star
Mass (M_\odot)	1.0	3.0×10^{-6}	1.5
Radius (km)	6.963×10^5	6.371×10^3	10
Orbital period (s)	2.33×10^6	8.64×10^4	10^{-3}
Equatorial velocity	6.26×10^{-6}	1.55×10^{-6}	0.21
Spin	1.18	8.89×10^2	0.379

Table 4. Spin and other physical properties of typical astrophysical objects

we see the effect of changing T_c and $r_{T,c}$ in the contours of $s_{\text{rms},*}/(v_{\text{eff},*}/A_s)$ in Fig. 14. Panel (d) shows the scan for the default choice $T_c = 10 \text{ MeV}$, $r_{T,c} = 0.4$. Panels (a) and (b) show the effect of changing T_c , which increases in value for larger T_c due to the increase in $g_{\rho,\text{SM}}$, consistent with Eq. (5.7). On the other hand, comparing panels (c) and (d) illustrates the effect of changing $r_{T,c}$, where a smaller $r_{T,c}$ increases the overall $s_{\text{rms},*}/(v_{\text{eff},*}/A_s)$.

5.3 Benchmarks

To obtain a general idea of the prediction for the RMS spin value of FV bubbles, we consider a collection of FOPT scenarios that will serve as our benchmark points. We require that these FOPT scenarios are, at least, physically viable. Then we calculate the transfer functions for these benchmarks, in order to eventually obtain $v_{\text{eff},*}$. One criterion we impose on these benchmarks is $T_*/T_c \leq 0.95$, which guarantees that the effective potential will have a sufficiently high barrier between the false vacuum and the true vacuum.

As usual, we had taken $A = 10^{-1}, 10^{-2}, 10^{-3}, 10^{-4}$; then for each A , we have selected $\lambda/\lambda_0(A) = 1.42, 2.34, 2.94, 5$. For each pair of (A, λ) , we scan over the physical region in the $L_c/T_c^4 - x_C$ plane and obtain physical quantities such as α_* , T_* , and $s_{\text{rms},*}/(v_{\text{eff},*}/A_s)$. We choose a random collection of FOPT scenarios and solve the perturbation equations to construct a table of transfer functions versus k/\mathcal{H}_c . This allows us to calculate \mathcal{C}_* and the effective equatorial velocity $v_{\text{eff},*}/A_s$, and finally $s_{\text{rms},*}$. The final benchmark points are presented in Table 1, with the rows organized in three groups. The first group (from the top) has parameters that specify the effective potential, critical temperature, and initial temperature ratio. The second group has quantities that can be obtained solely by tracking the evolution of the background cosmology during the phase transition. The third group has quantities that are relevant in inferring the features of the transfer functions, as well as quantities that can be obtained after solving the perturbation equations.

The benchmarks selected have notable features. Most of the benchmark points have $r_{T,c} = 0.4$. BP-1 and BP-3 have $T_c = 100 \text{ GeV}$, but correspond to different values of A . BP-1 and BP-2 have the same set of FOPT parameters $\{A, x_C, \lambda, L_c/T_c^4\}$ but BP-2 has a lower $T_c = 10 \text{ MeV}$. BP-5 corresponds to an FOPT with $T_c = 1 \text{ MeV}$. BP-8 has $T_c = 10 \text{ keV}$ and $r_{T,c} = 0.1$; it also gives the largest spin, while BP-6 features an FOPT with the smallest RMS spin among the benchmarks. Among the benchmarks, BP-7 has the lowest T_*/T_c , so that its rescaled elapsed time since the critical point $\tilde{\eta}_*$ is the longest among the benchmarks.

Comparing BP-1 and BP-2, which only differ in T_c , the change in RMS spin can be attributed to both the scaling in $(\beta/H_*)/v_{w,*}$, and in $g_{\rho,\text{SM}}$. In particular, while $g_{\rho,\text{SM}}$ decreased by around a factor of 10 from BP-1 to BP-2, $(\beta/H_*)/v_{w,*}$ increased by around a factor of 1.7; overall, the quantity $s_{\text{rms},*}/(v_{\text{eff},*}/A_s)$ only decreased by a factor of around 3. We emphasize that $(\beta/H_*)/v_{w,*}$ is roughly the inverse of the bubble radius relative to the

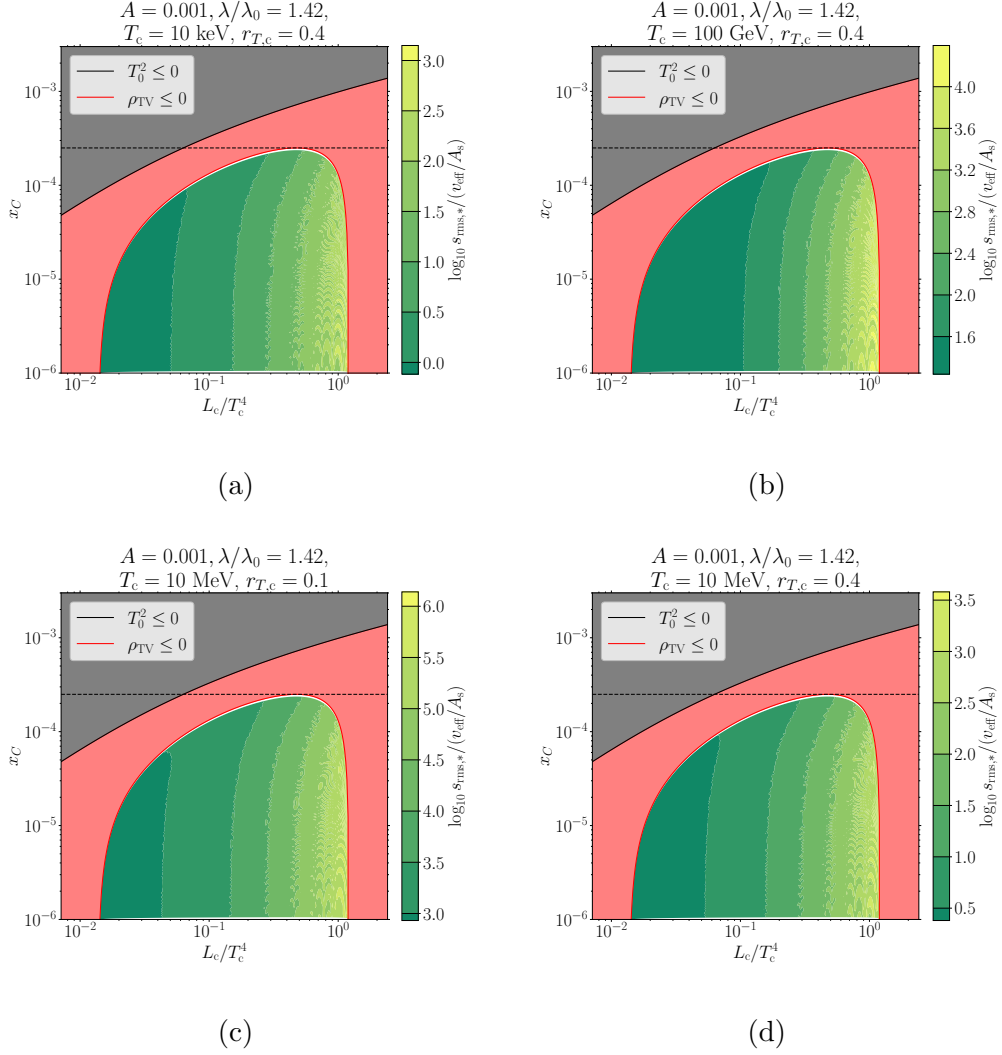


Figure 14. Contour plots of $s_{\text{rms},*}/(v_{\text{eff},*}/A_s)$ for $A = 10^{-3}$, changing T_c (top) and $r_{T,c}$ (bottom).

Hubble scale, according to Eq. (5.4), *i.e.* a larger $\sqrt{3}H_*R_*$ means a smaller $(\beta_*/H_*)/v_{w,*}$. A similar trend can be seen for BP-3 and BP-5, both with $A = 10^{-2}$, where a decrease of $\mathcal{O}(10)$ in $g_{\rho,\text{SM}}$ and an increase of $\mathcal{O}(1)$ in $(\beta/H_*)/v_{w,*}$ only leads to a decrease of $\mathcal{O}(1)$ in $s_{\text{rms},*}/(v_{\text{eff},*}/A_s)$. BP-4 and BP-5 have T_c at the MeV scale. Their $g_{\rho,\text{SM}}$ are both $\mathcal{O}(10)$, since the corresponding temperature in the SM sector is already below the QCD scale, where there is a marked decrease in the SM degrees of freedom. Analogously, their respective $(\beta_*/H_*)/v_{w,*}$ is $\mathcal{O}(10^3)$. The decrease in $s_{\text{rms},*}/(v_{\text{eff},*}/A_s)$ from BP-4 to BP-5 is mainly attributed to the increase in $r_{T,c}$ by a factor of 4, and is consistent with the scaling of $s_{\text{rms},*}/(v_{\text{eff},*}/A_s)$ as $r_{T,c}^{-4}$.

BP-6 provides the smallest RMS spin value in the whole table, and this is mainly due to its $(\beta_*/H_*)/v_{w,*}$ being the lowest in the whole table; equivalently, BP-6 has the largest $\sqrt{3}H_*R_*$ value in the table. In contrast, BP-8 has the smallest $\sqrt{3}H_*R_*$, so it has the largest $(\beta_*/H_*)/v_{w,*}$ ratio. Furthermore, $r_{T,c} = 0.1$ for BP-8, making its spin even larger. In principle, the RMS spins can be made higher by lowering the temperature ratio $r_{T,c}$; as a

trade-off, the phase transition strength becomes weaker.

6 Conclusions

Questions of how the angular momentum of primordial black holes is generated and how to characterize their spin distribution have been the subject of a lot of work. Most approaches assume an enhancement in the primordial curvature power spectrum in order to increase the probability of obtaining high peaks that can collapse to form primordial black holes. In contrast, the PBH formation mechanism we have in mind relies on dynamics during a first-order phase transition, which does not necessarily require an enhancement in the primordial curvature power spectrum. We restricted our calculation of the angular momentum and spin to the case of false vacuum bubbles. They can either collapse directly to PBHs or form Fermi balls that eventually collapse to PBHs. A minimal realization of the dark sector model consists of a singlet real scalar field, which triggers the FOPT by acquiring a nonzero vacuum expectation value through a temperature-dependent effective potential. To accommodate the Fermi ball formation scenario, we also introduce dark fermions which couple to the scalar field through a Yukawa interaction.

We adopted a picture in which the angular momentum is induced by cosmological perturbations, which ultimately come from initial Gaussian and nearly scale-invariant curvature perturbations. Taking the false vacuum bubbles to be spherical, we have reproduced the expected result that the leading-order contribution comes at second order in perturbations. Accounting for the FOPT in the dark sector, we tracked the evolution of cosmological perturbations up to the percolation time, where we wish to evaluate the angular momentum and spin. We ensured that the FOPT scenarios we considered are physical, such that the energy density in the true vacuum is positive, and where a minimum temperature exists at which there are two local minima in the effective potential.

We worked in the uniform Hubble gauge in tracking the evolution of cosmological perturbations during the FOPT, and numerically obtained the density, velocity, and metric perturbations for each Fourier mode within a chosen range of comoving wavenumbers. Carrying out this task requires knowledge of the evolution of the sound speed and equation of state of the tightly coupled dark fluid. In general, it is possible that the perturbations in the dark sector fluid may deviate from those of a pure radiation fluid, in cases where the equation of state and sound speed squared differ from $1/3$. In particular, we have found that the sound speed squared decreases around the time when the false vacuum fraction has a noticeable drop, takes a value smaller than $1/3$ at percolation, and then approaches the sound speed squared in the true vacuum. For subhorizon modes that have sufficiently short wavelengths, the density perturbations at the percolation time are enhanced relative to the ones in the case of density perturbations evolving in a pure radiation background. In contrast, velocity perturbations are suppressed. In the limit of extremely short-wavelength modes, the density and velocity perturbations at percolation are quenched to values that are determined by the sound speed at percolation. Once the perturbations at the percolation time are known, we calculate the RMS value of the angular momentum and spin. We performed this through phase-space integration, over pairs of Fourier modes, of a product of density and velocity perturbations weighted by a form factor associated with the size of the spherical false vacuum bubble.

From a classical mechanics standpoint, the RMS spin of the false vacuum bubble is dependent on the equatorial velocity, radius, and mass of the sphere. We have chosen the

radius of the FV bubble to be the maximal volume at the percolation time, within which no true vacuum bubble can nucleate. We have found a simple scaling relation, which relates the RMS spin with the inverse FOPT time scale β_*/H_* , the wall velocity, the degrees of freedom in the dark and SM sectors, and the initial dark-to-SM temperature ratio $r_{T,c}$. In particular, the RMS spin is mainly determined by $(\beta_*/H_*)/v_{w,*}$, $r_{T,c}$, and T_* . The RMS spin scales as $(\beta_*/H_*)^2/v_{w,*}^2$, and is inversely proportional to $r_{T,c}^4$. The quantity $(\beta_*/H_*)/v_{w,*}$ is mainly determined by the particular FOPT scenario. The critical temperature T_c also plays a role in determining the RMS spin, through the direct proportionality between $s_{\text{rms},*}$ and $g_{\rho,\text{SM}}$. We have found that the RMS spin value can take a wide range of values. For our sample scans with T_c between 10 keV and 100 GeV, and $r_{T,c}$ ranging from 0.1 to 0.4, it can be as low as $\mathcal{O}(10^{-3})$ to a few $\mathcal{O}(10^3)$. The upper limit on $r_{T,c}$ arises from the Planck constraint on the effective number of relativistic degrees of freedom, N_{eff} , and the lower limit on $r_{T,c}$ ensures that an FOPT occurs. A spin larger than unity does not pose any issue, since the false vacuum bubbles are not black holes.

Acknowledgments

We thank Pin-Jung Chen for collaboration during the early stages of this work. JTA thanks Reginald Bernardo, Daniel Harsono, Mehrdad Mirbabayi, Martin Spinrath, Yuhsin Tsai, and Ian Vega for fruitful discussions and insights. JTA and PYT acknowledge the kind support of the National Science and Technology Council of the Republic of China (formerly the Ministry of Science and Technology), with grant number NSTC 111-2811-M-007-018-MY2. DM acknowledges financial support from the U.S. Department of Energy under Grant No. DE-SC0010504. This work used high-performance computing facilities operated by the Center for Informatics and Computation in Astronomy (CICA) at the National Tsing Hua University. This equipment was funded by the Ministry of Education of Taiwan, the National Science and Technology Council of Taiwan, and National Tsing Hua University.

References

- [1] W.H. Press and P. Schechter, *Formation of galaxies and clusters of galaxies by selfsimilar gravitational condensation*, *Astrophys. J.* **187** (1974) 425.
- [2] A.M. Green, A.R. Liddle, K.A. Malik and M. Sasaki, *A New calculation of the mass fraction of primordial black holes*, *Phys. Rev. D* **70** (2004) 041502 [[astro-ph/0403181](#)].
- [3] S. Young and M. Musso, *Application of peaks theory to the abundance of primordial black holes*, *JCAP* **11** (2020) 022 [[2001.06469](#)].
- [4] C.-M. Yoo, T. Harada, S. Hirano and K. Kohri, *Abundance of Primordial Black Holes in Peak Theory for an Arbitrary Power Spectrum*, *PTEP* **2021** (2021) 013E02 [[2008.02425](#)].
- [5] M. Mirbabayi, A. Gruzinov and J. Noreña, *Spin of Primordial Black Holes*, *JCAP* **03** (2020) 017 [[1901.05963](#)].
- [6] V. De Luca, V. Desjacques, G. Franciolini, A. Malhotra and A. Riotto, *The initial spin probability distribution of primordial black holes*, *JCAP* **05** (2019) 018 [[1903.01179](#)].
- [7] T. Harada, C.-M. Yoo, K. Kohri, Y. Koga and T. Monobe, *Spins of primordial black holes formed in the radiation-dominated phase of the universe: first-order effect*, *Astrophys. J.* **908** (2021) 140 [[2011.00710](#)].
- [8] I.K. Banerjee and U.K. Dey, *Spinning Primordial Black Holes from First Order Phase Transition*, [2311.03406](#).

- [9] M.J. Baker, M. Breitbach, J. Kopp and L. Mittnacht, *Primordial Black Holes from First-Order Cosmological Phase Transitions*, [2105.07481](#).
- [10] C. Gross, G. Landini, A. Strumia and D. Teresi, *Dark Matter as dark dwarfs and other macroscopic objects: multiverse relics?*, *JHEP* **09** (2021) 033 [[2105.02840](#)].
- [11] K. Kawana and K.-P. Xie, *Primordial black holes from a cosmic phase transition: The collapse of Fermi-balls*, *Phys. Lett. B* **824** (2022) 136791 [[2106.00111](#)].
- [12] P. Lu, K. Kawana and K.-P. Xie, *Old phase remnants in first-order phase transitions*, *Phys. Rev. D* **105** (2022) 123503 [[2202.03439](#)].
- [13] M.W. Choptuik, *Universality and scaling in gravitational collapse of a massless scalar field*, *Phys. Rev. Lett.* **70** (1993) 9.
- [14] T.W. Baumgarte and C. Gundlach, *Critical collapse of rotating radiation fluids*, *Phys. Rev. Lett.* **116** (2016) 221103 [[1603.04373](#)].
- [15] T. Chiba and S. Yokoyama, *Spin Distribution of Primordial Black Holes*, *PTEP* **2017** (2017) 083E01 [[1704.06573](#)].
- [16] A. Heavens and J. Peacock, *Tidal torques and local density maxima*, *Monthly Notices of the Royal Astronomical Society* **232** (1988) 339.
- [17] T. Harada, C.-M. Yoo and K. Kohri, *Threshold of primordial black hole formation*, *Phys. Rev. D* **88** (2013) 084051 [[1309.4201](#)].
- [18] Y.N. Eroshenko, *Spin of primordial black holes in the model with collapsing domain walls*, *JCAP* **12** (2021) 041 [[2111.03403](#)].
- [19] J. Liu, L. Bian, R.-G. Cai, Z.-K. Guo and S.-J. Wang, *Constraining First-Order Phase Transitions with Curvature Perturbations*, *Phys. Rev. Lett.* **130** (2023) 051001 [[2208.14086](#)].
- [20] G. Elor, R. Jinno, S. Kumar, R. McGehee and Y. Tsai, *Finite Bubble Statistics Constrain Late Cosmological Phase Transitions*, [2311.16222](#).
- [21] C. Schmid, D.J. Schwarz and P. Widerin, *Amplification of cosmological inhomogeneities from the QCD transition*, *Phys. Rev. D* **59** (1999) 043517 [[astro-ph/9807257](#)].
- [22] L. Dolan and R. Jackiw, *Symmetry Behavior at Finite Temperature*, *Phys. Rev. D* **9** (1974) 3320.
- [23] G.W. Anderson and L.J. Hall, *The Electroweak phase transition and baryogenesis*, *Phys. Rev. D* **45** (1992) 2685.
- [24] L. Leitao and A. Megevand, *Hydrodynamics of phase transition fronts and the speed of sound in the plasma*, *Nucl. Phys. B* **891** (2015) 159 [[1410.3875](#)].
- [25] J.R. Espinosa, T. Konstandin, J.M. No and G. Servant, *Energy Budget of Cosmological First-order Phase Transitions*, *JCAP* **06** (2010) 028 [[1004.4187](#)].
- [26] F. Giese, T. Konstandin and J. van de Vis, *Model-independent energy budget of cosmological first-order phase transitions—A sound argument to go beyond the bag model*, *JCAP* **07** (2020) 057 [[2004.06995](#)].
- [27] T.V.I. Tenkanen and J. van de Vis, *Speed of sound in cosmological phase transitions and effect on gravitational waves*, *JHEP* **08** (2022) 302 [[2206.01130](#)].
- [28] L. Landau and E. Lifshitz, *The Classical Theory of Fields: Volume 2*, vol. 2, Butterworth-Heinemann (1975).
- [29] K.S. Thorne, J.A. Wheeler and C.W. Misner, *Gravitation*, Freeman San Francisco, CA (2000).
- [30] R.M. Wald, *General Relativity*, Chicago Univ. Pr., Chicago, USA (1984), [10.7208/chicago/9780226870373.001.0001](#).

- [31] E. Poisson, *A Relativist's Toolkit: The Mathematics of Black-Hole Mechanics*, Cambridge University Press (12, 2009), [10.1017/CBO9780511606601](#).
- [32] J.L. Jaramillo and E. Gourgoulhon, *Mass and Angular Momentum in General Relativity*, *Fundam. Theor. Phys.* **162** (2011) 87 [[1001.5429](#)].
- [33] A. Trautman, *Conservation laws in general relativity*, *Gravitation: An introduction to current research* (1962) 169.
- [34] P. Freud, *Über die ausdrücke der gesamtenergie und des gesamtimpulses eines materiellen systems in der allgemeinen relativitätstheorie*, *Annals of Mathematics* (1939) 417.
- [35] J.N. Goldberg, *Strong Conservation Laws and Equations of Motion in Covariant Field Theories*, *Phys. Rev.* **89** (1953) 263.
- [36] A. Komar, *Covariant conservation laws in general relativity*, *Phys. Rev.* **113** (1959) 934.
- [37] J. Katz, J. Bicak and D. Lynden-Bell, *Relativistic conservation laws and integral constraints for large cosmological perturbations*, *Phys. Rev. D* **55** (1997) 5957 [[gr-qc/0504041](#)].
- [38] C.-C. Chang, J.M. Nester and C.-M. Chen, *Pseudotensors and quasilocal gravitational energy momentum*, *Phys. Rev. Lett.* **83** (1999) 1897 [[gr-qc/9809040](#)].
- [39] A.N. Petrov and J. Katz, *Conserved currents, superpotentials and cosmological perturbations*, *Proc. Roy. Soc. Lond. A* **458** (2002) 319 [[gr-qc/9911025](#)].
- [40] J.M. Bardeen, *Gauge Invariant Cosmological Perturbations*, *Phys. Rev. D* **22** (1980) 1882.
- [41] H. Kodama and M. Sasaki, *Cosmological perturbation theory*, *Progress of Theoretical Physics Supplement* **78** (1984) 1.
- [42] J.-c. Hwang and H. Noh, *Relativistic hydrodynamic cosmological perturbations*, *General Relativity and Gravitation* **31** (1999) 1131.
- [43] P.J.E. Peebles, *Origin of the Angular Momentum of Galaxies*, *Astrophys. J.* **155** (1969) 393.
- [44] PLANCK collaboration, *Planck 2018 results. VI. Cosmological parameters*, *Astron. Astrophys.* **641** (2020) A6 [[1807.06209](#)].
- [45] N. Bartolo, V. De Luca, G. Franciolini, M. Peloso, D. Racco and A. Riotto, *Testing primordial black holes as dark matter with LISA*, *Phys. Rev. D* **99** (2019) 103521 [[1810.12224](#)].
- [46] S. Clesse, J. García-Bellido and S. Orani, *Detecting the Stochastic Gravitational Wave Background from Primordial Black Hole Formation*, [1812.11011](#).
- [47] V. Vaskonen and H. Veermäe, *Did NANOGrav see a signal from primordial black hole formation?*, *Phys. Rev. Lett.* **126** (2021) 051303 [[2009.07832](#)].
- [48] J.M. Bardeen, J.R. Bond, N. Kaiser and A.S. Szalay, *The Statistics of Peaks of Gaussian Random Fields*, *Astrophys. J.* **304** (1986) 15.
- [49] M. Shibata and M. Sasaki, *Black hole formation in the Friedmann universe: Formulation and computation in numerical relativity*, *Phys. Rev. D* **60** (1999) 084002 [[gr-qc/9905064](#)].
- [50] T. Harada, C.-M. Yoo, T. Nakama and Y. Koga, *Cosmological long-wavelength solutions and primordial black hole formation*, *Phys. Rev. D* **91** (2015) 084057 [[1503.03934](#)].
- [51] J.-c. Hwang, *Evolution of ideal fluid cosmological perturbations*, *Astrophys. J.* **415** (1993) 486.
- [52] M. Drees, F. Hajkarim and E.R. Schmitz, *The Effects of QCD Equation of State on the Relic Density of WIMP Dark Matter*, *JCAP* **06** (2015) 025 [[1503.03513](#)].
- [53] A.F. Heckler, *The Effects of electroweak phase transition dynamics on baryogenesis and primordial nucleosynthesis*, *Phys. Rev. D* **51** (1995) 405 [[astro-ph/9407064](#)].
- [54] A. Megevand, *Effect of reheating on electroweak baryogenesis*, *Phys. Rev. D* **64** (2001) 027303 [[hep-ph/0011019](#)].

- [55] W.-Y. Ai, B. Garbrecht and C. Tamarit, *Bubble wall velocities in local equilibrium*, *JCAP* **03** (2022) 015 [[2109.13710](#)].
- [56] W.-Y. Ai, B. Laurent and J. van de Vis, *Model-independent bubble wall velocities in local thermal equilibrium*, *JCAP* **07** (2023) 002 [[2303.10171](#)].
- [57] B. Kämpfer, *Phenomenological models of cosmic phase transitions. ii-application of the classical nucleation theory*, *Astronomische Nachrichten (ISSN 0004-6337)*, vol. 309, no. 6, 1988, p. 347-355. **309** (1988) 347.
- [58] F.C. Adams, *General solutions for tunneling of scalar fields with quartic potentials*, *Phys. Rev. D* **48** (1993) 2800 [[hep-ph/9302321](#)].
- [59] B. Kämpfer, *Phenomenological models of cosmic phase transitions*, *Astronomische Nachrichten (ISSN 0004-6337)*, vol. 309, no. 1, 1988, p. 19-24. **309** (1988) 19.
- [60] M.M. Flores, A. Kusenko and M. Sasaki, *Revisiting formation of primordial black holes in a supercooled first-order phase transition*, [2402.13341](#).
- [61] M.S. Turner, E.J. Weinberg and L.M. Widrow, *Bubble nucleation in first order inflation and other cosmological phase transitions*, *Phys. Rev. D* **46** (1992) 2384.
- [62] P. Athron, C. Balázs and L. Morris, *Supercool subtleties of cosmological phase transitions*, *JCAP* **03** (2023) 006 [[2212.07559](#)].
- [63] K. Enqvist, J. Ignatius, K. Kajantie and K. Rummukainen, *Nucleation and bubble growth in a first order cosmological electroweak phase transition*, *Phys. Rev. D* **45** (1992) 3415.